

Fast Ice Thickness Distribution in the Western Ross Sea in Late Spring

Patricia Jean Langhorne¹, Christian Haas², Daniel Price³, Wolfgang Rack⁴, Gregory H Leonard⁵, Gemma M. Brett³, and Stefano Urbini⁶

¹University of Otago

²AWI

³University of Canterbury

⁴University of Canterbury, NZ

⁵National School of Surveying

⁶Istituto Nazionale di Geofisica e Vulcanologia

December 7, 2022

Abstract

We present a 700 km airborne electromagnetic survey of late-spring fast ice and sub-ice platelet layer (SIPL) thickness distributions, from McMurdo Sound to Cape Adare, providing a first-time inventory of thickness close to its annual maximum. The overall modal consolidated ice (including snow) thickness was 1.9 m, less than its mean of 2.6 ± 1.0 m. Our survey was partitioned into level and rough ice, and SIPL thickness was estimated under level ice. Although results show a prevalence of level ice, with a mode of 2.0 m and mean of 2.0 ± 0.6 m, rough ice covered 41% of the transect by length, 50% by volume, with a mode of 3.3 m and mean of 3.2 ± 1.2 m. The thickest 10% of rough ice was almost 6 m on average, and a 2 km segment in Moubray Bay had a thickness greater than 8 m, demonstrating the overwhelming influence of deformation against coastal features. The fast ice was thus significantly thicker than adjacent pack ice. The presence of a significant SIPL was observed in Silverfish Bay, offshore Hells Gate Ice Shelf, New Harbour, and Granite Harbour where the SIPL transect volume was a significant fraction (0.30) of the consolidated ice volume. The thickest 10% of SIPLs had an average thickness of nearly 3 m, and near Hells Gate Ice Shelf the SIPL was almost 10 m thick, implying vigorous heat loss to the ocean ($\sim 90 \text{ W m}^{-2}$). We conclude that polynya-induced deformation and interaction with continental ice influence fast ice thickness in the western Ross Sea.

Fast Ice Thickness Distribution in the Western Ross Sea in Late Spring

P. J. Langhorne¹, C. Haas², D. Price³, W. Rack³, G. H. Leonard⁴, G. M. Brett³, and S. Urbini⁵

¹Department of Physics, University of Otago, Dunedin, New Zealand

²Alfred Wegener Institute for Polar and Marine Research, Bremerhaven, Germany

³Gateway Antarctica, University of Canterbury, Christchurch, New Zealand

⁴School of Surveying, University of Otago, Dunedin, New Zealand

⁵Istituto Nazionale di Geofisica e Vulcanologia, Roma, Italy

Corresponding author: Pat Langhorne (pat.langhorne@otago.ac.nz)

Key Points:

- Annual maximum fast ice & sub-ice platelet layer thickness distributions are surveyed by airborne electromagnetics over 700 km of Ross Sea (140 chars)
- Deformed against the coast, 50% of transect volume was rough first-year ice (mode 3.3 m thick), that was thicker than adjacent pack ice (138 chars).
- Sub-ice platelet layers over 0.5 m thick underlay level ice over large parts of four embayments, revealing land ice-fast ice interaction (139 chars).

Abstract

We present a 700 km airborne electromagnetic survey of late-spring fast ice and sub-ice platelet layer (SIPL) thickness distributions, from McMurdo Sound to Cape Adare, providing a first-time inventory of thickness close to its annual maximum. The overall modal consolidated ice (including snow) thickness was 1.9 m, less than its mean of 2.6 ± 1.0 m. Our survey was partitioned into level and rough ice, and SIPL thickness was estimated under level ice. Although results show a prevalence of level ice, with a mode of 2.0 m and mean of 2.0 ± 0.6 m, rough ice covered 41% of the transect by length, 50% by volume, with a mode of 3.3 m and mean of 3.2 ± 1.2 m. The thickest 10% of rough ice was almost 6 m on average, and a 2 km segment in Moubray Bay had a thickness greater than 8 m, demonstrating the overwhelming influence of deformation against coastal features. The fast ice was thus significantly thicker than adjacent pack ice. The presence of a significant SIPL was observed in Silverfish Bay, offshore Hells Gate Ice Shelf, New Harbour, and Granite Harbour where the SIPL transect volume was a significant fraction (0.30) of the consolidated ice volume. The thickest 10% of SIPLs had an average thickness of nearly 3 m, and near Hells Gate Ice Shelf the SIPL was almost 10 m thick, implying vigorous heat loss to the ocean ($\sim 90 \text{ W m}^{-2}$). We conclude that polynya-induced deformation and interaction with continental ice influence fast ice thickness in the western Ross Sea.

40

41

Plain Language Summary

Sea ice held stationary by the coast is named fast ice. Around Antarctica, it is often also observed near floating land ice and grounded icebergs. Fast ice is a critical habitat for marine life and known to be a sensitive indicator to changing weather and oceanic processes. Despite its importance, satellite measurements of its area are very recent, and hardly anything is known about its thickness. Using a specialized instrument on a fixed wing aircraft, we measured the 2017 November fast ice thickness in the western Ross Sea. Most of the ice surveyed was on average 2m thick and had formed in sheltered embayments. Where floating glaciers are in contact with fast ice, a 3-10m thick layer of loose ice crystals was sometimes observed beneath, which contributed to its thickness. However, most of the thicker ice was rough ice, formed when ferocious offshore winds pushed ice from the coast. It then drifted in the prevailing ocean currents until eventually becoming frozen in place against coastal topography. This rough ice, 3.3 m thick on average and comprising half the surveyed volume, was significantly thicker than adjacent freely-moving pack ice. Our survey provides a baseline from which future change can be measured.

57

58 1 Introduction

59 Antarctic land-fast sea ice (fast ice) is held stationary by the coastline, the seaward edge
60 of floating ice tongues or shelves, or by icebergs grounded in the shallow waters of the
61 continental shelf (Fraser et al., 2021; Giles et al., 2008). The seasonal loss of fast ice has been
62 shown to affect the stability of ice shelves (Massom et al., 2018) and glacier tongues (Stevens et
63 al., 2013; Gomez-Fell et al., 2022), hence also the Antarctic Ice Sheet coastal margins and outlet
64 glaciers (Massom et al., 2001). Fast ice is of major ecological importance (Mezgec et al., 2017)
65 as a breeding ground for species such as Weddell Seals (e.g., Ainley et al., 2015) and Emperor
66 Penguins (e.g., Jenouvrier et al., 2021), as a nursery for fish species (Vacchi et al., 2012) and as a
67 region of high primary productivity (Meiners et al., 2018). It is therefore imperative to
68 understand the processes influencing fast ice formation and distribution, and drivers of temporal
69 changes in the spatial coverage of fast ice.

70 Many factors are known to influence the distribution of fast ice (e.g., Fraser et al., 2021).
71 There is mutual interaction with coastal polynyas that affects the rate of sea ice production
72 through the rapid formation of frazil ice at the ocean surface (e.g., Tamura et al., 2016; Nakata et
73 al., 2021), and plays a role in sculpting the fast ice/pack ice edge (Nihashi and Ohshima, 2015).
74 Their margins represent areas of dynamic ice deformation (Rack et al., 2021; Hollands &
75 Dierking, 2016) and hence influence the development of the fast ice thickness distribution.

76 Marine-terminating continental ice also influences the coastal sea ice of Antarctica, with
77 platelet ice contributing to the fast ice cover through ice-ocean interaction (Hoppmann et al.,
78 2020; Langhorne et al., 2015). Melting at the base of ice shelves and outlet glaciers cools and
79 freshens the ice shelf-ocean boundary layer, producing Ice Shelf Water (ISW) with a potential
80 temperature below the surface freezing point (Foldvik and Kvinge, 1974; Jacobs et al., 1985). If
81 the ISW moves to shallower depths, the rise in its pressure-dependent freezing point may force it
82 to become supercooled in-situ, causing frazil crystals to persist in the water column. These ice
83 crystals may be deposited under ice shelves or ice tongues, and form marine ice (e.g., Tison et
84 al., 1998; Frezzotti, 1997). The frazil ice can grow into larger platelet ice crystals which add to
85 the mass of the coastal sea ice cover (e.g., Jeffries et al., 1993; Gow et al., 1998; Gough et al.,
86 2012). Under conditions outlined by Wongpan et al., (2021) the crystals form a porous, friable
87 layer, called the sub-ice platelet layer (SIPL) (Moreçki, 1965). The SIPL can be several metres
88 thick (e.g., Arndt et al., 2020; Hughes et al., 2014), with ground-based, single- and multi-
89 frequency electromagnetic induction measurements being used to map SIPL thickness, using
90 numerical inversion methods (Hunkeler et al., 2015; Brett et al., 2020). Consequently, platelet
91 ice formation not only causes sea ice to be thicker, but it also alters the hydrostatic relationship
92 between sea ice freeboard and thickness, influencing satellite altimeter determination of sea ice
93 thickness (Rack et al, 2013; Price et al., 2014; Arndt et al; 2020; Brett et al, 2021). Further, the
94 stabilization of the upper water column by basal ice shelf melt, or by an influx of surface ice
95 shelf meltwater (Bell et al., 2017), results in sea ice that is modelled to be ~ 0.2 m thicker than in
96 a well-mixed scenario (Hellmer, 2004; Kushara and Hasumi, 2014).

97 Progress has been made observing and understanding the factors controlling fast ice
98 extent (Fraser et al., 2020, 2021), but fast ice thickness remains a particular challenge. While
99 there are a few Antarctic embayments where the fast ice thickness distribution is well studied
100 (e.g., Arndt et al., 2020; Brett et al., 2020), Giles et al. (2008) have carried out a more extensive

101 study in east Antarctica using calibrated
 102 radar backscatter imaging to segregate
 103 fast ice into “smooth” and “rough”
 104 categories. They used proxy thicknesses
 105 of 1.7 m for “smooth” ice, and 5 m for
 106 “rough ice”, based on observations of
 107 multiyear fast ice near a glacier
 108 (Massom et al., 2001). Giles et al.
 109 (2008) indicate that 33 % of the fast ice
 110 is rough. Further they estimate that,
 111 although fast ice forms ~8 % of the
 112 total November sea ice (fast and pack
 113 ice) area for the studied sector of East
 114 Antarctica in 1997 and 1999, it may
 115 comprise almost 30 % of the total sea
 116 ice volume. Clearly the proportion of
 117 deformed ice in the fast ice cover is
 118 critical to an understanding of the
 119 overall fast ice thickness distribution.

120 Wide discrepancies still exist
 121 between Antarctic sea ice thickness
 122 estimates from satellite altimetry,
 123 largely due to the diversity of
 124 approaches to uncertainties in snow
 125 depth, and to the factors affecting the
 126 relationship between freeboard and ice
 127 thickness (e.g., Kacimi and Kwok,
 128 2020; Tian et al., 2020; Price et al.,
 129 2019). These problems are exacerbated
 130 for fast ice. At present, hemispheric-
 131 scale satellite investigations of fast ice
 132 thickness do not exist, because
 133 proximity to the coast presents
 134 challenges and the lack of open water
 135 makes it very difficult to identify sea
 136 level (Price et al., 2013; 2015; Brett et
 137 al., 2021). Thus the extensively-studied,
 138 large fast ice zone of McMurdo Sound is an excellent site for trialing techniques. Price et al.,
 139 (2013) used tide models in the derivation of satellite (ICESat) laser altimeter freeboards from
 140 2003 to 2009, and found freeboard was strongly linked to the development and incorporation of
 141 an SIPL. Radar altimeter (CryoSat-2) also detects annual fast ice freeboard trends in line with
 142 known sea-ice growth rates in McMurdo Sound (Price et al., 2015), while altimeter-derived
 143 thickness overestimates drill hole thickness because of buoyant forcing where there was a thick
 144 SIPL (Brett et al., 2021). The present study is motivated by the need for large-scale regional
 145 airborne measurements of fast ice thickness for comparison with satellite observations, and to

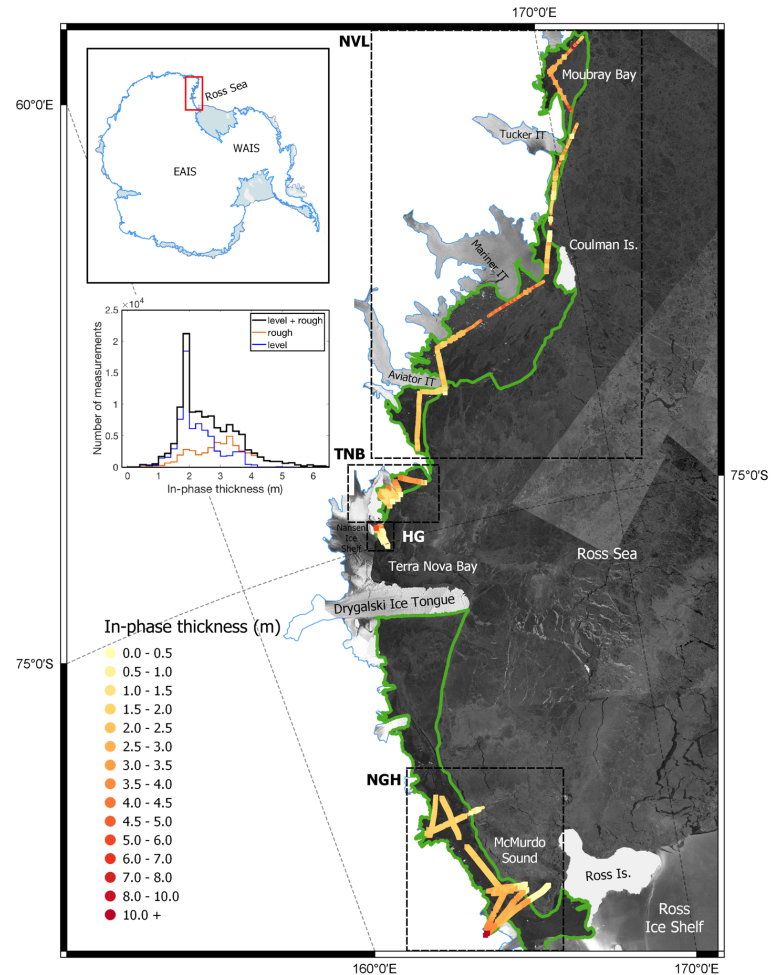


Fig. 1: In-phase apparent thickness (h_i), smoothed with 100 point median filter, for entire coastal survey displayed on Sentinel-1 Interferometric Wide (IW) swath mode image mosaic; images acquired between 10-20th November 2017. Level ice thickness is thicker line (squares), rough ice is thinner line (circles). Boxes show bounds of Figs 5 (NGH), 6 (HG), 7(TNB), 8 (NVL). Survey located on Antarctic overview map (top left). Fast ice edge indicated by green line. Histogram insert shows distribution of the level, rough and all in-phase apparent thicknesses of fast ice within the green ice edge.

146 better understand the coastal processes controlling fast ice distribution, including the partitioning
147 into rough, dynamic and level, thermodynamic growth.

148 In this study we use ice thickness data from airborne electromagnetic induction (AEM)
149 sounding (Haas et al., 2010) to study the fast ice thickness distribution in the western Ross Sea
150 within 30 days of its annual maximum extent (Fraser et al., 2021). Previous studies have
151 analysed AEM ice thickness surveys of pack ice in the western Ross Sea (Rack et al., 2021) and
152 of fast ice and SIPL within the confines of McMurdo Sound (Rack et al., 2013; Haas et al.,
153 2021). This is a first-time inventory of Antarctic fast ice thickness which can be used as baseline
154 for future studies and to better understand processes of fast ice formation, thickness, and
155 roughness. The particular questions being addressed are (i) what is the thickness distribution of
156 fast ice along the Victoria Land coast; (ii) what is the contribution of deformation to the fast ice
157 thickness and volume distributions; and (iii) where does a sub-ice platelet layer exist beneath the
158 fast ice, and what is its contribution to volume?

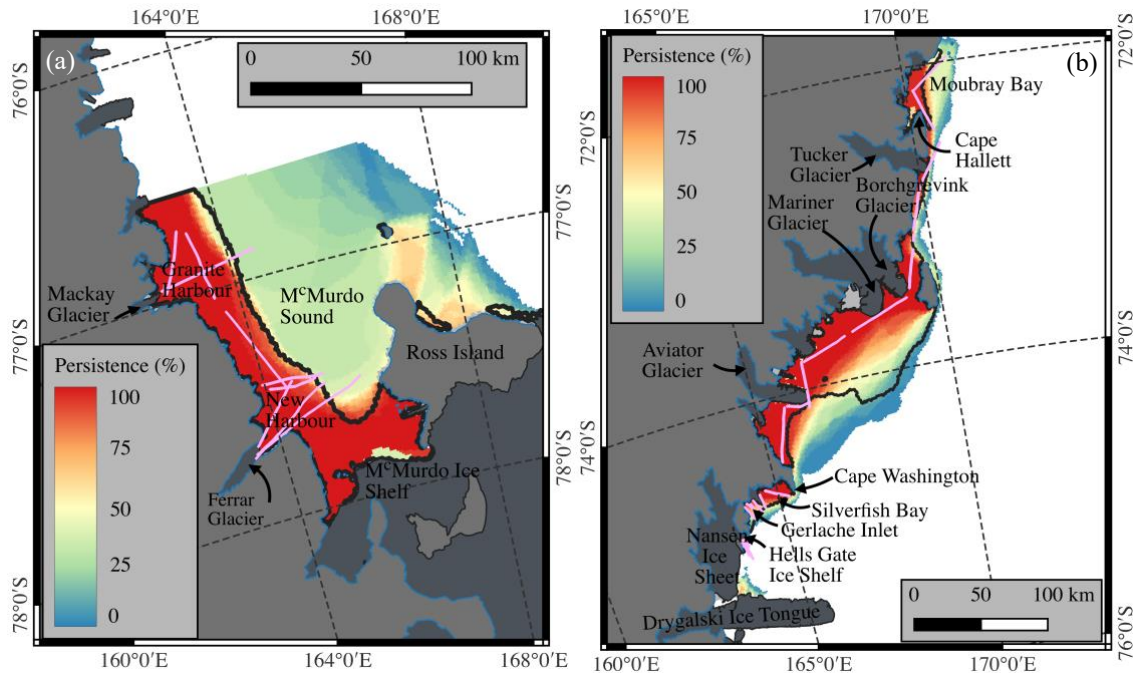
159 **2 The icescape of the Victoria Land coast**

160 The coastal sea ice of Victoria Land between the McMurdo Ice Shelf and Cape Adare
161 abuts 28 floating glaciers, ice tongues or ice shelves (Frezzotti, 1997), as indicated in Figs. 1 and
162 2. The Hells Gate and McMurdo Ice Shelves display substantial areas of marine ice accreted at
163 their base (Tison et al., 1998; Hoppmann et al., 2020), that sometimes reach the surface due to
164 wind-induced ablation (Frezzotti, 1997). The floating glaciers south of Terra Nova Bay calve
165 every few decades (Frezzotti, 1997) and are influenced by the presence or absence of fast ice
166 (e.g., Stevens et al., 2013; Han and Lee, 2018; Gomez-Fell et al., 2022). Some are toughened
167 against storms and wave action by marine ice at their base and within crevasses (Massom et al.,
168 2018). Thus interaction between continental ice and fast ice is a common feature of the Victoria
169 Land coast, and we expect frazil/platelet ice and an SIPL to be present in some fast ice regions.

170 The western Ross Sea is also notable for polynya activity, with fast ice persistence, ice
171 transport and ISW formation driven by the complex interaction among three significant
172 polynyas: the Ross Sea polynya (in front of the Ross Ice Shelf), the Terra Nova Bay polynya and
173 the McMurdo Sound polynya (e.g., Rack et al., 2020). The Ross Sea Polynya produces High
174 Salinity Shelf Water (HSSW), generating ISW formation which flows into McMurdo Sound, and
175 then northwards in a coherent coastal current that is conjectured to flow along the Victoria Land
176 coast (Stevens et al., 2017; Jendersie et al., 2018). HSSW is also generated by opening events of
177 the Terra Nova Bay Polynya (e.g., Fusco et al., 2009; Yoon et al., 2020), influencing fast ice
178 persistence and ice transport along the coast. The McMurdo Sound Polynya influences the fast
179 ice edge in McMurdo Sound (e.g., Leonard et al., 2021).

180 The thickness distribution of an SIPL is largely conditioned by ocean heat flux (e.g.,
181 Lewis and Perkin, 1985; Langhorne et al., 2015; McPhee et al., 2016; Wongpan et al., 2021).
182 Evidence for the cold, coherent, northward-moving current (Stevens et al., 2017) links our study
183 area to the extensively studied ISW plume of McMurdo Sound (e.g., Lewis and Perkin, 1985;
184 Barry, 1988; Mahoney et al., 2011; Robinson et al., 2014), with its resulting SIPL thickness
185 distribution (e.g., Gow et al., 1998; Hughes et al., 2014; Price et al., 2014; Haas et al., 2021).
186 These studies showed that an SIPL occurs in a 20 to 30 km wide, 40 to 80 km long region
187 extending from the northern tip of the McMurdo Ice Shelf in a north-westerly direction. At the
188 end of winter the thickness of the SIPL under first year ice can be up to 7.5 m (Price et al., 2014;
189 Hughes et al., 2014), coinciding with more than 2.5 m of consolidated sea ice. The distribution of

190 the SIPL in McMurdo Sound is remarkably consistent from year to year under fast ice
 191 (Langhorne et al., 2015), with inter-annual variability related to polynya activity (Brett et al.,
 192 2020).



193
Fig. 2: Map of coastline of (a) McMurdo Sound to Granite Harbour and (b) Victoria Land north of 75°S (cf. Fig. 1). Fast ice persistence in November taken from Fraser et al. (2020) dataset for 2000-2018. Ice shelves and tongues shown in dark grey. Light grey pixels are the terrestrial ice mask from Fraser et al. (2020). Fast ice edge determined by Fraser et al. (2020) for 12 November 2017 indicated by black line. AEM flight lines between 8 & 13 November 2017 shown in magenta.

194
 195 The thickness distribution of an SIPL is largely conditioned by ocean heat flux
 196 (e.g., Lewis and Perkin, 1985; Langhorne et al., 2015; McPhee et al., 2016; Wongpan et al.,
 197 2021). Evidence for the cold, coherent, northward-moving current (Stevens et al., 2017) links our
 198 study area to the extensively studied ISW plume of McMurdo Sound (e.g., Lewis and Perkin,
 199 1985; Barry, 1988; Mahoney et al., 2011; Robinson et al., 2014), with its resulting SIPL
 200 thickness distribution (e.g., Gow et al., 1998; Hughes et al., 2014; Price et al., 2014; Haas et al.,
 201 2021). These studies showed that an SIPL occurs in a 20 to 30 km wide, 40 to 80 km long region
 202 extending from the northern tip of the McMurdo Ice Shelf in a north-westerly direction. At the
 203 end of winter the thickness of the SIPL under first year ice can be up to 7.5 m (Price et al., 2014;
 204 Hughes et al., 2014), coinciding with more than 2.5 m of consolidated sea ice. The distribution of
 205 the SIPL in McMurdo Sound is remarkably consistent from year to year under fast ice
 206 (Langhorne et al., 2015), with inter-annual variability related to polynya activity (Brett et al.,
 207 2020).

208 Terra Nova Bay is bordered by the Drygalski Ice Tongue to the south and by the
 209 Campbell Ice Tongue to the north (see Fig. 2). The Drygalski Ice Tongue acts as a barrier for
 210 pack ice advection from the south and the south-west, whilst katabatic winds blow offshore and

211 sporadically keep the Terra Nova Bay polynya area ice free (e.g., Fusco et al., 2009). The
212 Drygalski Ice Tongue is also a barrier to the proposed northward-flowing cold current (Stevens
213 et al, 2017). In Terra Nova Bay itself marine ice and ISW are common features (e.g., Frezzotti,
214 1997; Tison et al., 1998; Budillon and Spezie, 2000; Yoon et al., 2020). A wind-driven cyclonic
215 gyre dominates the upper ocean of Terra Nova Bay (Van Woert et al., 2001), directing surface
216 currents mainly north-east along the coast (Budillon and Spezie, 2000). Close to the coast, Terra
217 Nova Bay Ice Shelf Water (TISW) arises due to the interaction of the shallow–intermediate
218 layers of HSSW with the coastal glaciers (Budillon and Spezie, 2000). In addition TISW near the
219 Nansen Ice Shelf is advected northwards with the cyclonic circulation (Yoon et al., 2020). The
220 fast ice of the region is strongly affected by ISW, forming platelet ice (Vacchi et al., 2012).

221 The Hells Gate Ice Shelf is a small ice shelf separated from the Nansen Ice Shelf by
222 Inexpressible Island (Fig. 2). It is composed almost entirely of marine ice (Souchez et al., 1991;
223 Tison et al., 1998) due to high surface ablation combined with basal accretion of sea water. It is
224 well known that the sea ice in front of the Hells Gate Ice Shelf is heavily influenced by locally-
225 and regionally-generated ISW (Tison et al., 1998).

226 In the northern part of our study area (see Figs. 1 and 2) there is less information on the
227 fast ice and the extensiveness of its interaction with marine-terminating ice bodies. Moubray Bay
228 is a location of almost year-round fast ice in the western Ross Sea (Ainley et al., 2015), and the
229 timing of freeze-up and breakup during the 21st century does not differ significantly from that in
230 the 1960s in Moubray Bay (Ainley et al., 2015; Fraser et al., 2020).

231 **3 Methods**

232 3.1 Instrumentation and area of investigation

233 The AEM survey flights took place on 8, 9, 10 and 13 November 2017, with coastal
234 flight tracks shown in Fig. 1. The study area extended 700 km along the Victoria Land coast of
235 the western Ross Sea from New Harbour (77.7°S, 164.0°E) to near the Adare Peninsula (72.0°S,
236 171.5°E).

237 The AEM surveys were carried out with an EM sensor (“EM Bird”) towed beneath a
238 Basler BT67 aircraft, a turbo DC3. The EM Bird was flown with an average speed of 120 knots
239 at mean heights of 16 m above the ice surface (Haas et al., 2010). It was operated in vertical
240 dipole mode with a signal frequency of 4060 Hz and a spacing of 2.67 m between transmitting
241 and receiving coils (Haas et al., 2009). The sampling frequency was 10 Hz, corresponding to a
242 sample spacing of approximately 6 m. A Riegl LD90 laser altimeter was used to measure the
243 Bird's height above the snow/ice surface, with a range accuracy of ± 0.025 m (Haas et al., 2021).
244 At this height the footprint of the AEM measurements is about 45 m. Georeferenced photographs
245 were taken of the snow/ice surface from an altitude of 100 m with an aircraft-mounted Canon
246 EOS 5D Mark III nadir-looking camera with a 24 mm lens.

247 The single-frequency AEM measurements record in-phase and quadrature signals
248 representing the amplitude and phase of the induced secondary field relative to the primary field
249 transmitted by the EM Bird. Over level ice and in the absence of an SIPL, total (snow plus ice)
250 thicknesses determined from in-phase and quadrature measurements agree within an accuracy of
251 ± 0.10 m (Haas, 2004; 2006; Haas et al., 2009; Pfaffling et al., 2007). In rougher ice the
252 maximum thickness of pressure ridges or rubble fields is generally underestimated due to their
253 three-dimensional shape and porosity, resulting in up to 50% underestimation of the “true”

254 thickness of unconsolidated ridges (e.g., Pfaffling et al., 2007; Haas & Jochmann, 2003). As we
 255 do not know the snow thickness, we assume that it is similar throughout the study region and less
 256 than 10% of the total ice thickness (Fons and Kurtz, 2019). In what follows, we treat level ice as
 257 a 3-layer system (snow+consolidated ice, the sub-ice platelet layer (SIPL) and sea water) and
 258 retrieve the thickness of the SIPL in addition to that of snow+ice (e.g., Rossiter and Holladay,
 259 1994; Haas et al., 2021).

260 3.2 Identifying the sub-ice platelet layer

261 From multiple years of AEM measurements over level fast ice in McMurdo Sound, a
 262 method has been developed to find the thickness of the high porosity/higher conductivity sub-ice
 263 platelet layer, h_{sipl} , at the base of the sea ice (Haas et al., 2021). Beneath level ice, the porous
 264 SIPL causes a deviation of the in-phase- and quadrature-derived retrievals. In that case, we call
 265 the AEM-derived thicknesses *apparent thickness*, as they differ from the “true” thickness of fully
 266 consolidated ice of negligible conductivity (Haas et al., 2021). In the presence of an SIPL, the
 267 in-phase-derived apparent thickness (from now on termed in-phase apparent thickness) is greater
 268 than the true consolidated ice thickness, but less than the thickness of the consolidated ice plus
 269 SIPL (Haas et al., 2009; Rack et al., 2013). On the other hand, the apparent quadrature-derived
 270 thickness (from now on called quadrature apparent thickness) is less affected by the presence of
 271 a SIPL (Haas et al., 2021) and is close to the “true” thickness. Thus the thickness of the SIPL
 272 can be derived from the difference between the apparent in-phase and quadrature thicknesses.

273 However, due to the low signal-to-noise ratio of the quadrature signals, SIPL data are
 274 very noisy and smoothing is necessary. Over level fast ice typical SIPL thickness variations are
 275 sufficiently gradual that smoothing does not remove information. Therefore, unless stated
 276 otherwise, here we first smoothed apparent in-phase and quadrature thickness data with a 100
 277 point median filter; i.e., smoothed over approximately 600 m. Then, following Haas et al. (2021),
 278 h_{sipl} is found using

$$279 \quad h_{sipl} \approx (h_I - h_Q) / \alpha$$

280 where h_I and h_Q are the apparent thickness of the in-phase and quadrature measurements
 281 respectively, and the SIPL scaling factor, $\alpha = 0.4$, was determined by calibrating against drill
 282 hole thickness measurements in McMurdo Sound in November 2017 (Haas et al., 2021). The
 283 uncertainty in SIPL thickness of ± 0.5 m is greater than that of typically ± 0.1 m in consolidated
 284 ice thickness (Haas et al., 2021).

286 In extensive deformed ice and rubble fields, the blockiness of the ice keels also results in
 287 porous layers which affect the EM signal in a similar way to the SIPL, again causing the in-
 288 phase- and quadrature-derived apparent sea ice thicknesses to deviate (Fig. 3). Consequently the
 289 SIPL cannot be found unambiguously under rough ice. We overcome this additional challenge
 290 by distinguishing level from rough ice, and calculating SIPL thickness only under level ice.

291 3.3 Discriminating level ice from rough ice

293 Numerous methods have been used to distinguish level ice from deformed, rough ice
 294 (e.g., Wadhams and Horne, 1980; Giles et al., 2008; Beckers et al., 2017; Tin and Jeffries, 2001;
 295 Rabenstein et al., 2010; Von Albedyll et al., 2021). Here we identified sections of level ice from

296 rough ice by modifying the method of Rabenstein et al. (2010) and Von Albedyll et al. (2021).
 297 We find the absolute value of the point-by-point, unsmoothed, vertical, in-phase thickness
 298 gradient, $\Delta h_I/\Delta x$, and smooth it over 101 points (approximately 600 m of profile length) using a
 299 centered moving median filter. Level ice is defined where the filtered gradient is smaller than
 300 0.006, a value chosen by Von Albedyll et al. (2021). Allowing for small variations in flight
 301 speed, we conservatively take the minimum possible separation between along-profile samples,
 302 Δx , as 5 m, while Δh_I is the difference in unsmoothed, in-phase apparent thickness between
 303 adjacent EM measurements. Thus ice is categorized as level at position n if

304

$$305 \widehat{\Delta h_I(n)} = \text{median} \{ \Delta h_I(n - M), \dots, \Delta h_I(n + M) \} < (0.006 \times 5 \text{ m}) = 0.03 \text{ m}$$

306

307 where $M = 50$. Rough ice is defined where

308

$$309 \widehat{\Delta h_I(n)} \geq 0.03 \text{ m}$$

310

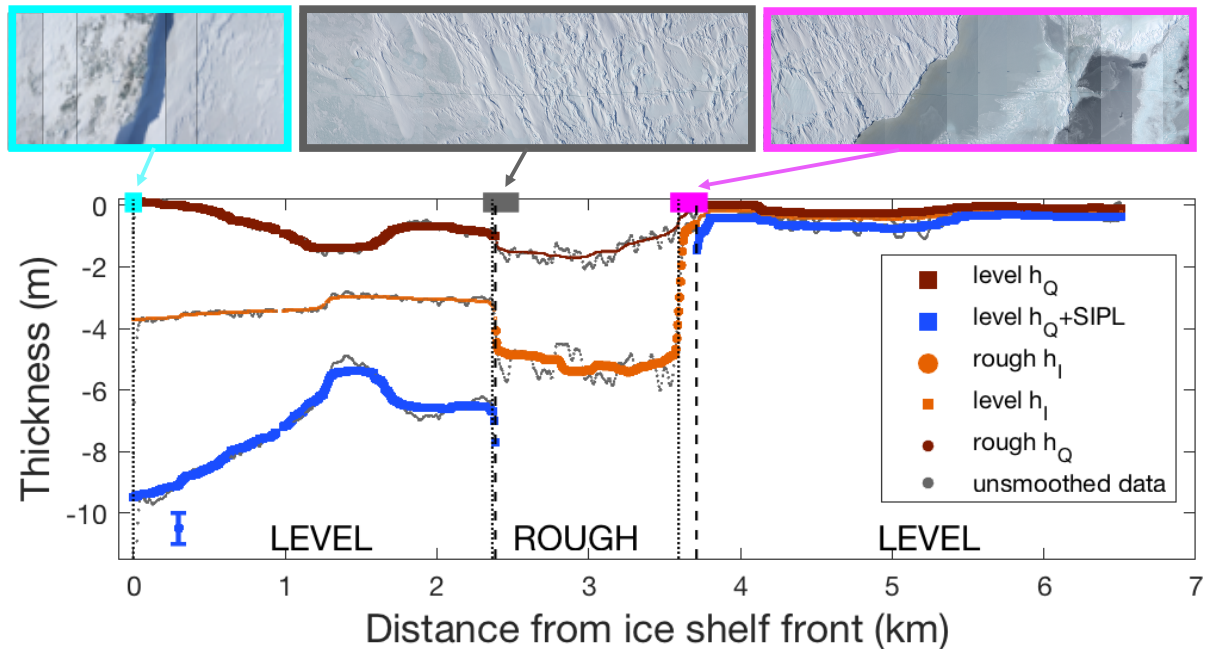
311 Assuming that the AEM sample points, Δx , are equidistant and that the width of the AEM
 312 footprint does not change during the survey, the fraction of transect length, L , and fraction of
 313 transect volume, V , that are level or rough are respectively defined as

$$314 L = \frac{N_k}{N} \text{ and } V = \frac{\sum_{k=1}^{N_k} h_k}{\sum_{i=1}^N h_i}$$

315

316 where N is the total number of samples in the transect, N_k the number of thickness samples from
 317 either level or rough ice, and h is the respective thickness (Rack et al., 2021).

318 Aerial photographs were taken from the aircraft at an altitude of approximately 100 m
 319 above the ice to verify the robustness of the rough-ice detection algorithm. Fig. 3 demonstrates
 320 the verification of transitions between ice types just offshore from the Hells Gate Ice Shelf. The
 321 maximum lateral difference between the transition identified by the algorithm, and that identified
 322 visually from aerial photographs, is of the order of 200 m, and generally less than 50 m. Fig. 3
 323 also illustrates that in this section of the survey the in-phase and quadrature apparent thicknesses
 324 differ by several meters over both rough and level ice. As discussed above, this difference results
 325 from a porous layer under the ice, but we are unable to distinguish between blocks of ice in
 326 rubble keels and an SIPL. Consequently in this paper we take the conservative approach of
 327 reporting only in-phase apparent thickness under rough ice, i.e. we do not attempt to infer the
 328 presence and thickness of an SIPL. In contrast, under level ice the quadrature apparent thickness
 329 represents the consolidated snow+ice thickness and an SIPL can be calculated with an
 330 uncertainty of ± 0.5 m (Haas et al., 2021). Our chosen measures over level and rough ice are
 331 denoted by larger symbols in Fig. 3 (appearing as thicker lines).



332

Fig 3: Illustration of identification of rough and level ice and the SIPL off the Hells Gate Ice Shelf (on left). Thicknesses are shown downwards from snow/ice surface at 0 m, plotted against distance from ice shelf front. In-phase and quadrature apparent thicknesses under rough (circles) and level (squares) fast ice are compared. Unsmoothed data in grey. All other data are smoothed with 100 point median filter. Quadrature apparent thickness (h_Q) in brown, quadrature plus SIPL in blue (uncertainty indicated by bar), and in-phase apparent thickness (h_I) in orange. Under level ice h_Q represents the consolidated ice thickness, while for rough ice h_I is the best measure, as denoted by larger symbols. Photo mosaics of sea ice surface features, showing transitions from ice shelf to nearshore level ice (cyan), from nearshore level to rough ice (grey), and from rough to pack ice (magenta). Boundaries identified from aerial photographs (dotted) and roughness algorithm (dashed) shown as vertical lines.

333

334

3.4 Delineating the boundary between fast ice and pack ice

335

336

337

338

339

340

341

342

343

344

345

346

347

In November 2017 the area covered by land-fast sea ice in the Ross Sea was 2% of the total sea ice area (Li et al., 2020), typical of the eight Novembers examined in the Li et al. study. Fraser et al. (2020, 2021) have recently produced a continuous, high spatio-temporal resolution (1 km, 15 d) time series of circum-Antarctic fast ice extent from March 2000 to March 2018 (see Fig. 2 and Fig. S11 for this dataset in the western Ross Sea). Fig. 2 shows the likelihood of finding fast ice in a pixel during the month of November over the years 2000 to 2018 (Fraser et al., 2020), with flight tracks from the present survey superimposed. In this paper, Fraser et al. (2020) is the primary guide to identify the fast ice edge. Then, as a secondary guide, we use Sentinel-1 and MODIS imagery on the days of the AEM surveys to delineate fast ice from pack ice at a more suitable resolution for the EM thickness surveys. We also ensure that all ice present in the fast ice dataset has persisted for at least 15 days, and is mechanically fastened to shoreline features.

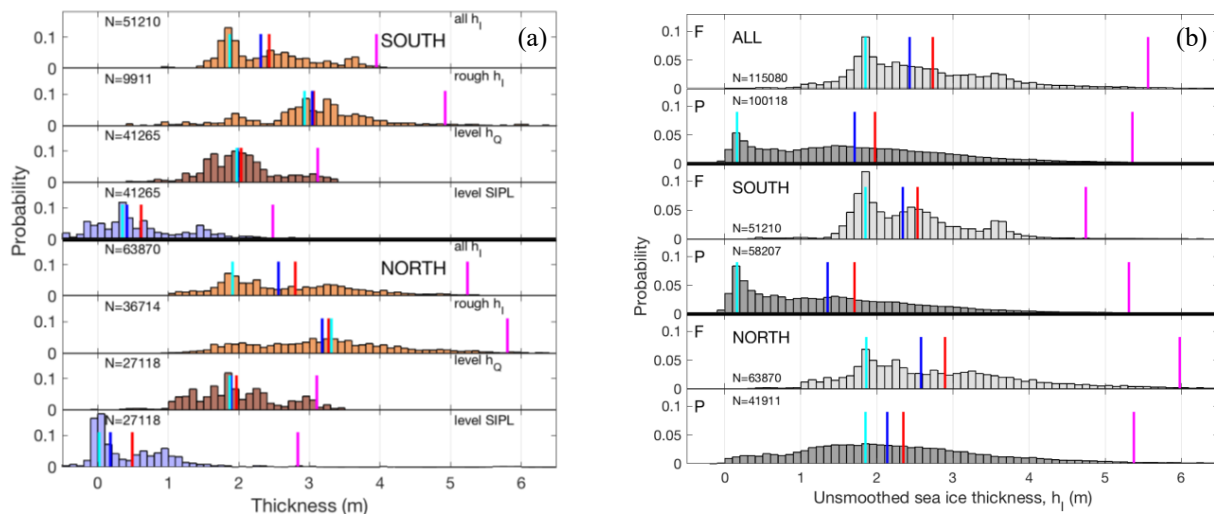
348 **4 Results**

349

350

4.1 Fast ice statistics of western Ross Sea

351 The fast ice extent in November 2017 (see Fig. 2) was typical of November 2000-2018
 352 (Fraser et al., 2020), as illustrated in Fig SII. An examination of MODIS visual imagery from
 353 October 2016 to April 2017 implies that most of the surveyed fast ice was first-year ice, with
 354 open water observed at some time during summer along most of the AEM survey lines. Only
 355 within 9 km of the front of the Ferrar Glacier in New Harbour (see Fig. 1) did the fast ice remain
 356 in place through the summer of 2016/2017. Rack et al. (2021) have provided a description of
 357 events immediately preceding the observed coastal and fast ice thickness distributions of
 358 November 2017. In the absence of strong wind events, pack ice in the area generally drifts
 359 northwards. A strong polynya event on 4 October 2017 pushed ice towards the northwest from
 360 the Ross Sea and McMurdo Polynyas towards the Drygalski Ice Tongue, and towards Terra
 361 Nova Bay (left panel of Fig. 1 in Rack et al.). After this event, the ice drifted to the northeast
 362 again (right panel of Fig. 1 in Rack et al.). Events like this created the rough ice in front of Hells
 363 Gate Ice Shelf, and on the margins of the fast ice of Silverfish Bay (see Fig. 1). Multiple such
 364 events occur every year, sculpting the fast ice edge.



365

Fig. 4(a): Probability distributions of 100-point median filtered fast ice thicknesses in western Ross Sea in November 2017. Upper four panels show ‘south of 75°S’, lower four panels ‘north of 75°S’. Panels show all in-phase apparent thicknesses h_1 in orange, rough h_1 in orange, level h_Q in brown, and SIPL in blue. The mean (red), median (blue), mode (cyan) and h_{H10} (magenta) bars are shown for each distribution. The number of samples (N) in each dataset is given.

(b) Probability distributions of unsmoothed in-phase apparent thicknesses (h_1) in the western Ross Sea in November 2017, comparing fast ice with pack ice from Rack et al. (2021). Top two panels compare all fast ice (F) with all pack ice (P) thicknesses. Fast ice (F) and pack ice (P) data ‘south of 75°S’ and ‘north of 75°S’ are compared in the middle and bottom two panels, respectively. The mean (red), median (blue), mode (cyan) and h_{H10} (magenta) bars are shown for each distribution. The number of samples (N) in each dataset is given.

366

367 **Table 1: Statistics of fast ice thickness in western Ross Sea, c.f. Fig 4a**368 * h_Q is not determined in less than 0.07% cases where h_I is found.369 h_{H10} is the mean of the thickest 10% of ice thicknesses.

Section	Number of meas.	$h_{\text{mean}} \pm \text{standard deviation (m)}$	$h_{\text{mode (m)}}$	$h_{\text{median (m)}}$	$h_{\text{max (m)}}$	$h_{H10 (m)}$	L (%)	V (%)
ALL								
fast ice traversed (h_I)	115080	2.63±1.03	1.87	2.42	11.40	4.78		
rough (h_I)	46625	3.22±1.19	3.31	3.15	11.40	5.66	41	50
level consolidated (h_Q)	68383*	2.01±0.58	1.97	1.95	4.40	3.11	59	50
level SIPL	68383*	0.56±1.01	0.05	0.37	9.64	2.67		
SOUTH of 75°S								
fast ice traversed (h_I)	51210	2.43±0.76	1.87	2.31	6.65	3.95		
rough (h_I)	9911	3.05±0.96	2.93	3.04	6.65	4.92	19	24
level consolidated (h_Q)	41265*	2.03±0.54	1.97	1.98	3.79	3.12	81	76
level SIPL	41265*	0.61±0.91	0.35	0.41	5.64	2.48		
NORTH of 75°S								
fast ice traversed (h_I)	63870	2.80±1.18	1.91	2.56	11.40	5.24		
rough (h_I)	36714	3.27±1.25	3.31	3.18	11.40	5.80	58	67
level consolidated (h_Q)	27118*	1.97±0.62	1.87	1.89	4.40	3.10	42	33
level SIPL	27118*	0.49±1.15	0.02	0.18	9.64	2.84		

370
371 Fig. 1 shows the in-phase apparent thickness of all the coastal sea ice surveyed (including
372 minor fractions of pack ice immediately adjacent to the fast ice edge) in November 2017. In
373 addition, the in-phase thicknesses are separated into level and rough ice, using the algorithm
374 described in section 3.3. Of more than 800 km of coastal sea ice (fast and pack) surveyed,
375 approximately 700 km was over fast ice, of which 59% by transect length (50% by transect
376 volume) was level ice (see Table 1). In this paper we focus on the ice within the fast ice
377 boundary defined as described in section 3.4, which removes ice less than 0.1 m thick indicative
378 of new ice or open water in polynyas and leads adjacent to the fast ice edge (see insert of Fig. 1).

379 Table 1 and Fig. 4 report statistics for two regions of similar number of data points.
380 “South of 75°S”, includes New Harbour and Granite Harbour (NGH box in Fig. 1) but excludes
381 any McMurdo Sound data reported elsewhere (Haas et al., 2021). “North of 75°S” includes the
382 sea ice in front of the Hells Gate Ice Shelf (HG box in Fig. 1); the Gerlache Inlet/Silverfish Bay
383 region of Terra Nova Bay (TNB box in Fig. 1), in addition to a 400 km transect up the coastline
384 of northern Victoria Land from Cape Washington to Cape Adare (box NVL in Fig. 1).

385 The modal thickness of all level fast ice surveyed was 2.0 m (mean = 2.0±0.6m) (see
386 Table 1 & Fig. 4), consistent with first year thermodynamic fast ice formation in the area (e.g.,
387 Leonard et al., 2006). Noting the uncertainty of ±0.5 m in SIPL thickness determination, under
388 level ice an SIPL was found in some areas with an overall mean of 0.6±1.0 m and mode = 0.1 m
389 (see Table 1 & Fig. 4a). This disguises the fact that in some locations the SIPL may be up to
390 almost 10 m thick, and the thickest 10% has an average thickness of 2.7 m (Table 1). The modal
391 thickness of the rough ice was 3.3 m (mean = 3.2±1.2 m, Table 1 & Fig. 4a), with a maximum
392 fast ice thickness of over 11 m in Moubray Bay at the northern end of the survey (Table 1).

393 **Table 2: Statistics of pack ice thickness (unsmoothed data from Rack et al., 2021) from**
 394 **western Ross Sea, November 2017 compared with fast ice thickness (unsmoothed from**
 395 **present work), c.f. Fig 4b**

396 h_{H10} is the mean of the thickest 10% of ice thicknesses.

Section	Number of meas.	$h_{\text{mean}} \pm$ standard deviation (m)	h_{mode} (m)	h_{median} (m)	h_{max} (m)	h_{H10} (m)
ALL						
fast ice traversed (h_f)	115080	2.73 \pm 1.30	1.85	2.43	24.80	5.56
pack ice traversed (h_p)	100118	1.97 \pm 1.56	0.16	1.71	15.58	5.36
SOUTH of 75°S						
fast ice traversed (h_f)	51210	2.53 \pm 1.10	1.85	2.34	24.80	4.75
pack ice traversed (h_p)	58207	1.71 \pm 1.59	0.16	1.35	11.78	5.31
NORTH of 75°S						
fast ice traversed (h_f)	63870	2.90 \pm 1.43	1.86	2.58	19.60	5.98
pack ice traversed (h_p)	41911	2.35 \pm 1.44	1.85	2.14	15.58	5.38

397
 398 As anticipated the mode of the thermodynamically-grown, level fast ice in the north is
 399 thinner than in the south, but only by 0.1 m (1.9 m cf 2.0 m in Table 1 & Fig. 4a). However
 400 overall the northern ice has a mean that is 0.4 m thicker (2.8 m cf 2.4 m in Table 1 & Fig. 4a)
 401 because of the higher proportion of rough, deformed ice in the north (58% cf 19% by length in
 402 Table 1).

403 In Table 2 we compare our fast ice data with the pack ice thickness offshore, surveyed at
 404 the same time and reported in Rack et al. (2021). In this case, unsmoothed, in-phase apparent
 405 thickness data are used for pack and fast ice as these are appropriate for pack ice data. The mean
 406 and median of the 700 km survey of fast ice thicknesses are approx. 0.7 m (~30-40%) greater
 407 than the 800 km survey of pack ice in the same region (see Table 2 and Fig. 4b), while the mode
 408 is more than 1.5 m greater in the fast ice. Thus, while the area covered by fast ice is small, its
 409 contribution to sea ice volume is significant.

410

411 4.2 Results and discussion of subregions.

412 In the following we split the survey into segments, moving south to north. There are four
 413 embayments: New Harbour and Granite Harbour (NGH box in Fig. 1); in front of the Hells Gate
 414 Ice Shelf (HG box); the Gerlache Inlet/Silverfish Bay region of Terra Nova Bay (TNB box), in
 415 addition to a 400 km transect up the coastline of northern Victoria Land from Cape Washington
 416 to Cape Adare (box NVL in Fig. 1).

417 4.2.1 Granite Harbour & New Harbour (NGH)

418 While the sea ice in the area was mostly first year ice, within 9 km of the front of the
 419 Ferrar Glacier in New Harbour there was ice that had persisted throughout the summer
 420 2016/2017 (see Fig. 5c), where the transition can be seen from second year ice of about 3.0 m
 421 thickness, to first year ice of 2.1 m. The fast ice in this area was influenced by the grounded
 422 tabular iceberg shown in Figs. 5a&b, which had been in this approximate position and
 423 orientation since March 2014. All fast ice in Granite Harbour had been in place for less than 8

424 months. Granite Harbour and New Harbour (Figs. 5a&b) are regions where platelet ice has
 425 previously been reported as a casual reference to its presence within some other study (e.g.,
 426 Stockton, 1983; SooHoo et al., 1987; Barry, 1988; Cummings et al, 2019).

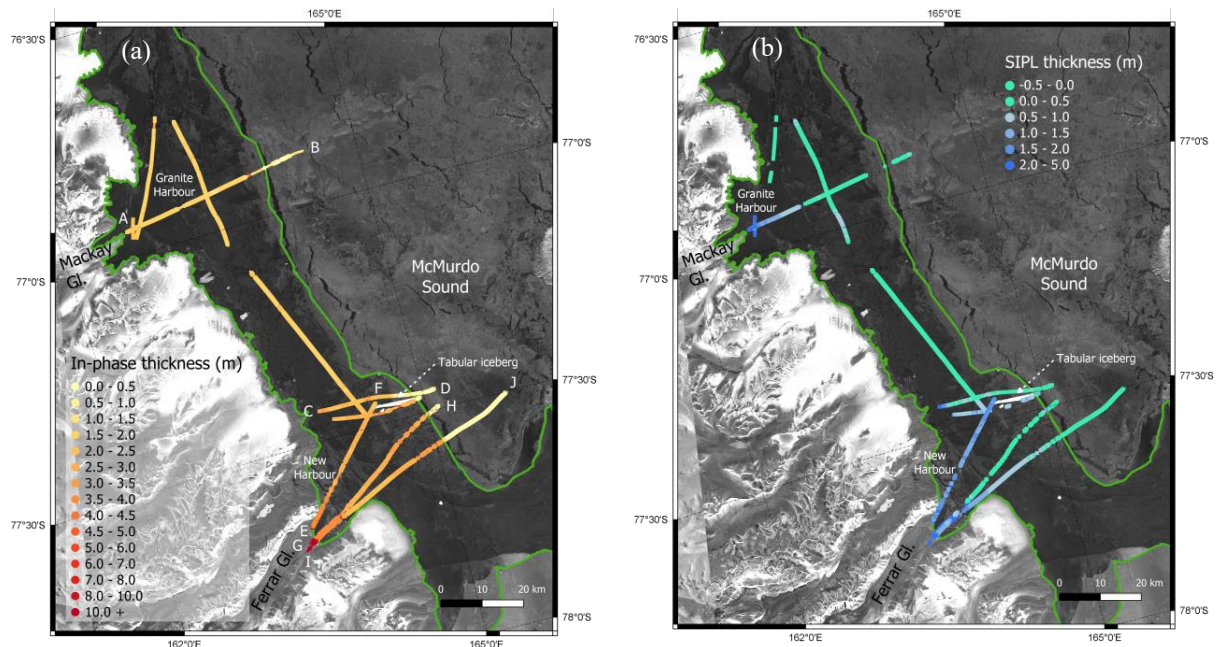


Fig 5: New Harbour and Granite Harbour. **(a)** In-phase apparent thickness (h_i) plotted on Sentinel-1 Interferometric Wide (IW) swath mode image acquired 14 November 2017 2122 UTC. Locations A-J identified. Level ice shown as thicker line (squares), rough ice as thinner line (circles). Fast ice edge indicated by green line. **(b)** As (a) but for SIPL thickness under level ice. **(c)** Five transects bounded by locations A-J, plotted against distance from coastal end of transect. Thickness measured downwards from snow/ice surface at zero. Consolidated level ice thickness (h_0) in brown, and consolidated ice thickness plus SIPL in blue (uncertainty indicated by bar in panel E-F). Rough ice thickness (h_1) in orange. Second year ice shaded pink, regions outside the fast ice edge shaded grey.

427
 428
 429
 430
 431
 432
 433
 434
 435
 436
 437

Here level ice comprised 81% of the cover by length (see Fig. 5 and Table 1 SOUTH). The modal thickness of the consolidated level ice was 2.0 m, consistent with thermodynamically-grown first-year fast ice (e.g., Leonard et al., 2006); its mean was 2.0 ± 0.5 m. The mean SIPL thickness of 0.6 ± 0.9 m was considerably larger than the mode of 0.3 m, indicating a skewed distribution with a maximum of 5.6 m (Table 1 SOUTH). Fig. 5b demonstrates that generally the SIPL was thicker close to the coast and towards the south. A possible source of ISW to maintain this SIPL distribution is the proposed coherent current that moves northwards from the McMurdo Ice Shelf to beyond Granite Harbour (Stevens et al., 2017).

438 However, local sources may also contribute to platelet ice formation. Five approximately
439 east-west transects of Fig. 5a&b have been plotted in Fig. 5c. The decrease in SIPL is evident,
440 from between 2 and 5 m thick at the coastal edge, to approximately zero at the outer fast ice
441 edge. The exception is transect E-F where an SIPL approx. 1.5 m thick was observed along the
442 entire length of the transect. This transect was closest to the location (at label 'New Harbour' in
443 Fig. 5a) of previous observations of ice crystals beneath multi-year sea ice (Murray et al., 2013),
444 and close to submarine ice cliffs at the mouth of the Taylor Valley (Stockton, 1983; Murray et
445 al., 2013). This implication of supercooled water, along with the inferred existence of anchor ice
446 at the head of the Ferrar Glacier (Mager et al., 2013), suggests that the glacier terminus of the
447 Ferrar may be a local source of supercooled water providing km-scale spatial variations in SIPL
448 thickness. In particular, the 3 m thick SIPL at location A (see Figs. 5a&b) is 120 km distant from
449 the McMurdo Ice Shelf as a potential source of ISW. The SIPL is more likely sourced beneath
450 the floating tongue of the Mackay Glacier (Debenham, 1965; Frezzotti, 1997). Formation of an
451 SIPL around a floating glacier tongue is not unprecedented, such observations having been
452 reported around the Erebus (Stevens et al., 2014) and Drygalski (Stevens et al., 2017) ice
453 tongues.

454 Alternatively, underwater ice crystal formation may be caused by the double diffusive
455 effects of cold, saline brines entering the ocean through subsurface connections with inland
456 lakes, aquifers, and subglacial waters (Foley et al., 2019). Such connections have been identified
457 beneath the Ferrar Glacier, where subglacial brines have been shown to have an open connection
458 directly into the Ross Sea, and at the submarine ice cliffs where Lake Fryxell in the lower Taylor
459 Valley is connected to a deeper aquifer beneath the lake to the Ross Sea (Foley et al., 2019).
460 Extreme halophiles have been observed in New Harbour, supporting the hypothesis of this
461 submarine discharge (Currie et al., 2021).

462

463 4.2.2 Sea ice in front of Hells Gate Ice Shelf (HG)

464 In the vicinity of the Hells Gate Ice Shelf, three distinct regions are identified on radar
465 images, aerial photos and ice thickness data (Figs. 3 & 6). The SAR images of Fig. 6a and b
466 show level sea ice close to the ice shelf, bounded to the south by a triangular-shaped region of
467 rough ice (Zhai et al., 2019). This ice was first year ice, much of which became established
468 around 25 September (from time series of MODIS images and Zhai et al., 2019), just prior to the
469 deformation event discussed above. The exceptions were first-year ice shoreward of the dashed
470 lines in Fig. 6a, and a narrow border of multi-year ice (< 500 m wide) hugging the eastern coast
471 of the embayment, that survived through summer 2016/2017. This multi-year ice was not
472 surveyed in November 2017.

473 Our results show that the relatively thin, just over one month old, level ice had a mean
474 thickness of 1.1 ± 0.3 m, underlain by a substantial SIPL of thickness 3.4 ± 2.2 m (Figs. 6b&c).
475 That is, the fast ice grew to about 1.1 m thick in 45 days, implying a spectacularly high average
476 growth rate of 2.5 cm d^{-1} . We surmise that this level ice was protected by the triangular-shaped
477 region of rough ice, and grew rapidly with heat extracted to the atmosphere by katabatic winds
478 and to the ocean by supercooled ISW. Heat fluxes will be estimated in the Discussion.

479

480

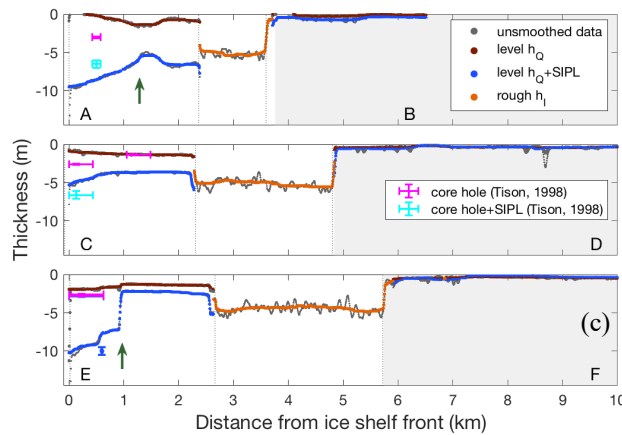
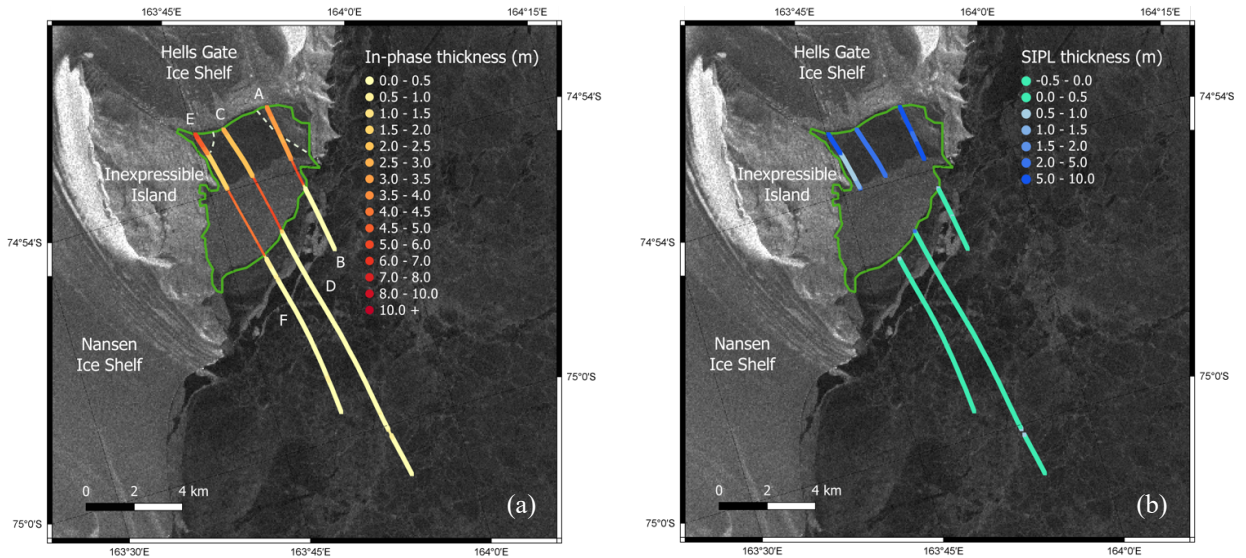


Fig 6: Sea ice in front of Hells Gate Ice Shelf
(a) In-phase apparent thickness (h_i) plotted on Sentinel-1 Interferometric Wide (IW) swath mode image acquired 10 November 2017 1029 UTC. Locations A-F identified. Level ice shown as thicker line (squares), rough ice as thinner line (circles). Fast ice edge indicated by green line. Ice older than 45 days is coastward of dashed pale green line.
(b) As (a) but for SIPL thickness under level ice.

(c) Three transects, bounded by locations A-F, plotted against distance from ice shelf front. Thickness measured downwards from snow/ice surface at zero. Unsmoothed data shown in grey. All other data smoothed with 100 point median filter. Consolidated level ice thickness (h_Q) in brown, and consolidated ice thickness plus SIPL in blue (uncertainty indicated by bar in panel E-F). Rough ice thickness (h_i) in orange. Vertical dotted lines indicate boundaries identified from aerial photographs (see Fig 3 for transect A-B). Regions outside the fast ice shaded in grey, ice older than 45 days coastward of green arrows. Core lengths of consolidated sea ice (magenta) and with estimates of SIPL (cyan) for January 1994 and October 1995 (Tison et al., 1998).

481
 482
 483
 484
 485
 486
 487
 488
 489
 490

Providing a barrier that protects the level ice, the rough ice was a very thick rubble field (see airborne camera mosaic in Fig. 3) deformed by wind-driven compression against the coast. Time series of MODIS images confirm that it formed sometime between September 30 and October 5 (Zhai et al., 2019), during the same coastward deformation event on 4 October reported by Rack et al. (2021). Thus the rough ice had likely been in place for just over a month at the time of the survey. Its mean thickness was 4.7 ± 0.6 m, with a mode of 4.4 m, in agreement with a single, December 2017, ice-breaker observation of 3–4 m in the vicinity of our location F (Zhai et al., 2019). Unlike the thinner ice towards the ice shelf, this feature was only present four

491 times between 2003–2017 (Zhai et al., 2019), and we speculate that it may be related to the
 492 increased activity in the Terra Nova Bay polynya, as noted for 2017 by Yoon et al. (2020). The
 493 thin ice (mean = 0.3 ± 0.1 m) seaward of the deformed ice in the outer fast ice zone (Fig. 6 a&c)
 494 was newly formed nilas ice, as can be seen in Fig. 3.

495 Our airborne measurements agree well with earlier on-ice observations. Tison et al.
 496 (1998) reported platelet ice in first year land-fast sea ice in front of the Hells Gate Ice Shelf in
 497 January 1994 and October 1995. There is considerable uncertainty in the relative positions
 498 because, in the two decades between the Tison et al. (1998) observations and our AEM surveys,
 499 we estimate that the ice shelf front would have advanced ~ 80 m in the east (A-B in Fig. 6c) and
 500 300-400 m in the west (E-F in Fig. 6c).

501 In October 1995 Tison et al. (1998) reported an ice core with a length of 1.35 m in close
 502 agreement with the AEM consolidated ice thickness (see middle panel Fig. 6c) at a site ~ 1.2 km
 503 along transect C-D. Further, Tison et al. (1998) report “large amounts of loose frazil” beneath the
 504 fast ice where our present estimate is an SIPL of 2.4 m. In January 1994, Tison et al. (1998)
 505 sampled eight core holes from first year fast ice at a distance of 50 – 150 m from the ice shelf
 506 front. Remarkably, the pattern of platelet ice accumulation along the ice shelf front in spring
 507 2017 concurs with that of Tison et al.’s (1998) summer observations two decades earlier. They
 508 report “no significant amount of loose ice crystals” in the section of the transect on the western
 509 side of the ice shelf front. This is consistent with an SIPL of less than 1 m between 1 and 2.5 km
 510 from the ice shelf front on transect E to F (see bottom panel Fig. 6c). In contrast, in the east “a
 511 thick layer of about 3-4 m” was observed by Tison et al. (1998), consistent with our SIPL
 512 observation beyond 1 km from the ice shelf front of 2.5 – 5 m from A-B and C-D.

513

514 4.2.3 Gerlache Inlet and Silverfish Bay, Terra Nova Bay (TNB)

515 Seven flight transects (~ 76 km in total) were conducted over Gerlache Inlet and
 516 Silverfish Bay in northern Terra Nova Bay, a sheltered bay in which first-year fast ice forms
 517 annually (Fig. 2a). Gerlache Inlet is partially separated from Silverfish Bay by the Campbell
 518 Glacier Tongue (see Fig. 7a), a fast-flowing glacier that is grounded near the ice front at its
 519 southwestern end (Han et al., 2022). Ice thickness was measured in 14 drill holes in November
 520 2017 in Gerlache Inlet. Good agreement was found with our in-phase apparent thicknesses h_I
 521 (see Fig. 7a). No platelet ice was recorded in the drill holes (see Fig. 7a&c) and the AEM survey
 522 confirms SIPL was thin in Gerlache Inlet (see Fig. 7b).

523 This region was ice free in late February/early March 2017 and in-phase apparent
 524 thickness, shown in Fig. 7a, is consistent with thermodynamically-grown, 8 months old, first
 525 year fast ice. There are significant portions of level ice (72% of the cover by length) allowing
 526 SIPL thickness to be determined (Fig. 7b). Here level fast ice had a mean thickness of 2.1 ± 0.8 m.
 527 The rough fast ice was only slightly thicker (mean = 2.3 ± 0.7 m) implying that there is relatively
 528 little deformed ice or ice older than first year in the embayment. The 2017 observed median ice
 529 thickness of 2.3 m is thinner than median values of Vacchi et al. (2012) in 2005 and 2006, who
 530 found consolidated ice median thicknesses from drill holes lay between 2.4 and 2.8 m during
 531 surveys for Antarctic silverfish eggs. The discrepancy between 2005/2006 and 2017 thicknesses
 532 probably reflects the fact that our survey extended to the fast ice edge, while theirs was
 533 concentrated closer to the coast. Fig. 7a confirms the increase in sea ice thickness towards the

534 coast. Although no detailed sea ice or SIPL thickness distributions are available, in 2005/2006
 535 the thickest consolidated fast ice consistently appears to be to the east of the Campbell Ice
 536 Tongue (Vacchi et al., 2012).

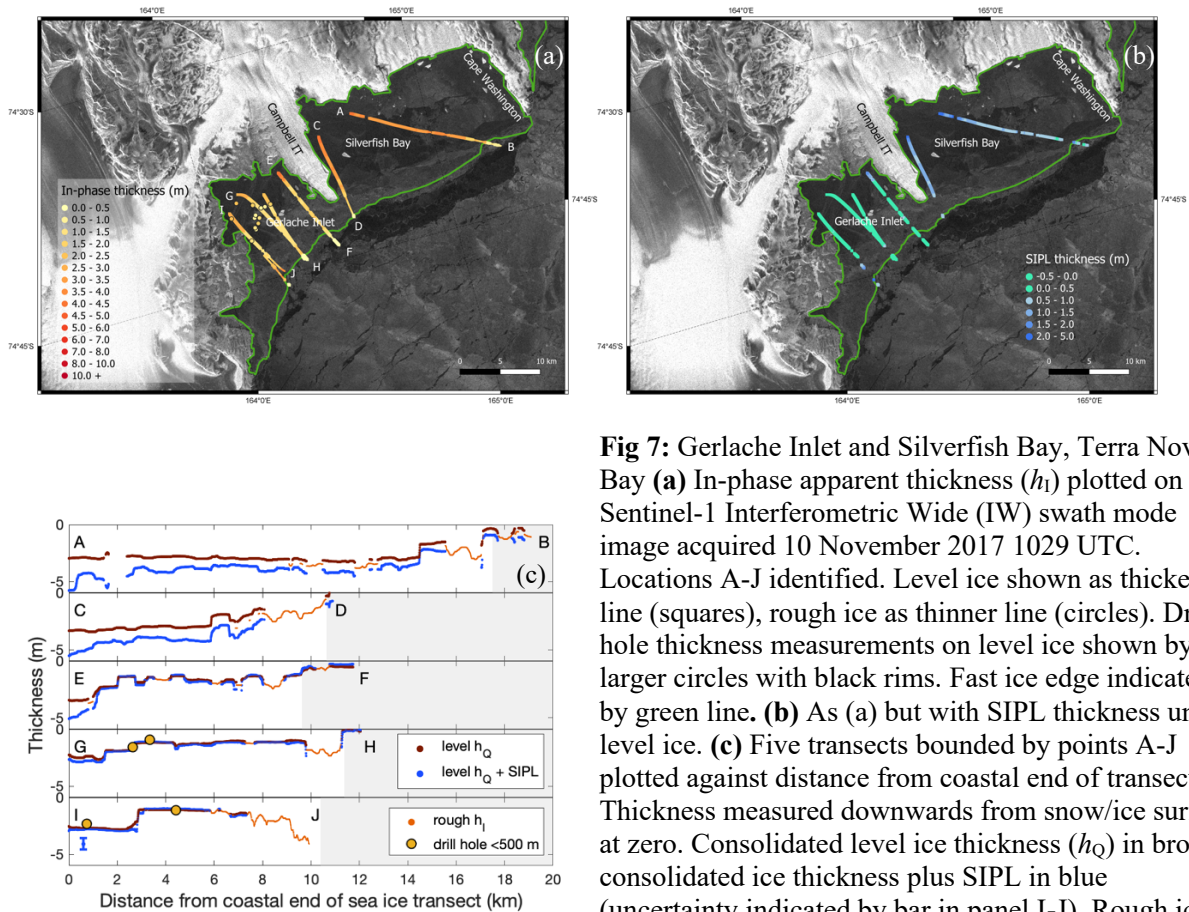


Fig 7: Gerlache Inlet and Silverfish Bay, Terra Nova Bay **(a)** In-phase apparent thickness (h_1) plotted on Sentinel-1 Interferometric Wide (IW) swath mode image acquired 10 November 2017 1029 UTC. Locations A-J identified. Level ice shown as thicker line (squares), rough ice as thinner line (circles). Drill hole thickness measurements on level ice shown by larger circles with black rims. Fast ice edge indicated by green line. **(b)** As (a) but with SIPL thickness under level ice. **(c)** Five transects bounded by points A-J plotted against distance from coastal end of transect. Thickness measured downwards from snow/ice surface at zero. Consolidated level ice thickness (h_Q) in brown, consolidated ice thickness plus SIPL in blue (uncertainty indicated by bar in panel I-J). Rough ice thickness (h_1) in orange. Orange circular symbols with black rim are drill hole measurements within 500 m of transects. Regions outside fast ice edge shaded grey.

537

538 An SIPL was definitively detected by the airborne survey, confirming qualitative
 539 observations of the occurrence of platelet ice in 37% of drill holes in 2005 and 88% in 2006
 540 (Vacchi et al., 2012). The consolidated ice thickness and thickness with the SIPL of the five
 541 longest transects (~64 km) are shown in Fig. 7c. The thickest SIPLs were observed to the east of
 542 the Campbell Ice Tongue, (in Silverfish Bay and west of Cape Washington) with SIPLs of 2.8 m
 543 and 2.1 m at A and C respectively at the coastal ends of these profiles (see Fig. 7 b&c). On the
 544 eastern side of the Campbell Ice Tongue (C-D in Fig. 7) the maximum SIPL thickness of 2.1 m
 545 decreases to just beneath 1 m about 3 km from the coastal end of the transect. However this 1 m-
 546 thick SIPL then persisted along the 8 km surveyed. By contrast on the western side of the
 547 Campbell Ice Tongue, in Gerlache Inlet, the SIPL is thinner. Here, the maximum of 1.6 m
 548 decreases to less than 0.5 m within 1.2 km (see Fig. 7b & c). Perhaps this implies that the
 549 Campbell Ice Tongue is the source of supercooled water that is swept eastward by the cyclonic
 550 ocean currents (Van Woert et al, 2001, Yoon et al., 2020).

551

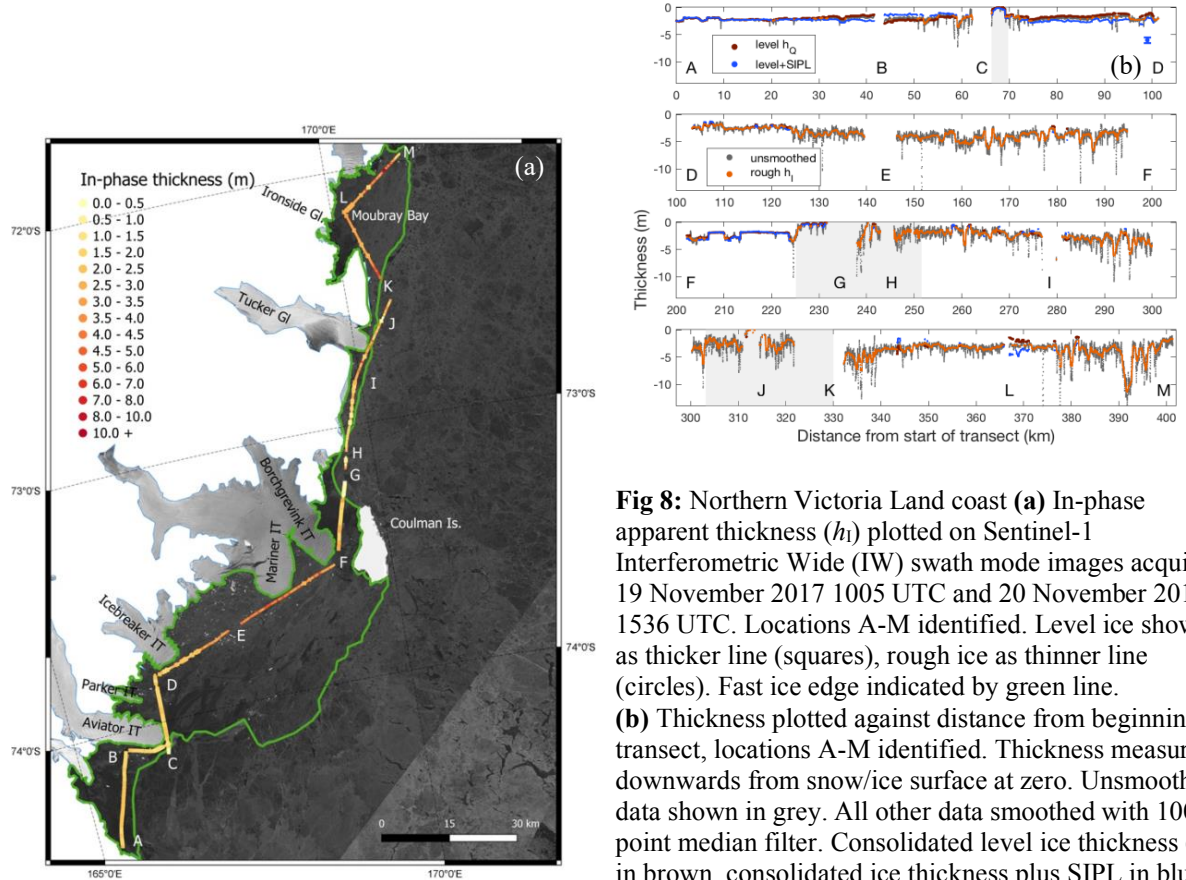


Fig 8: Northern Victoria Land coast (a) In-phase apparent thickness (h_i) plotted on Sentinel-1 Interferometric Wide (IW) swath mode images acquired 19 November 2017 1005 UTC and 20 November 2017 1536 UTC. Locations A-M identified. Level ice shown as thicker line (squares), rough ice as thinner line (circles). Fast ice edge indicated by green line. (b) Thickness plotted against distance from beginning of transect, locations A-M identified. Thickness measured downwards from snow/ice surface at zero. Unsmoothed data shown in grey. All other data smoothed with 100 point median filter. Consolidated level ice thickness (h_Q) in brown, consolidated ice thickness plus SIPL in blue (uncertainty indicated by bar in top panel). Rough ice thickness (h_r) in orange. Regions outside the fast ice edge shaded in grey.

552
 553
 554
 555

4.2.4 North Victoria Land coast (NVL)

556 The transect from Cape Washington to Cape Adare passed some substantial glacier
 557 tongues (see Fig. 8a), however, the SIPL had a modal thickness of 0.2 ± 0.7 m;
 558 the smallest value of any of our selected regions. The level fast ice (see example in Fig SI2a) had
 559 a mean thickness of 1.9 ± 0.4 m (mode=1.9 m), thinner than that to the south (mode = 2.0 m).
 560 However only 35% of the transect was level ice (Fig. 8b). Rough ice occupied 65% of this 400
 561 km stretch of coast by transect length (75% by transect volume) with a mean thickness of
 562 3.3 ± 1.2 m. As a result, the mean thickness of the fast ice (level+rough) was 2.9 ± 1.2 m (see Fig.
 563 8a&b), the thickest of the four regions identified and thicker than the expected thermodynamic
 564 thickness in November, emphasizing the important role of deformation on the fast and pack ice
 565 in this region. Indeed a maximum thickness in excess of 11 m was encountered towards the
 566 northern end of the transect, where the thickness consistently exceeded 8 m along a 2 km stretch
 567 in Moubray Bay (see Fig. 8a & section L to M of Fig 8b & photograph of b). Inspection of
 568 MODIS images suggests that this feature had been incorporated into the fast ice cover for about

569 7 months and was possibly thick pack ice floes (Rack et al., 2021), or fragments of the previous
570 disintegrating fast ice cover (Hollands & Dierking, 2016).

571 There was also highly deformed ice between E & F (Fig. 8b) with an average thickness of
572 4.0 m along a 47 km portion of transect. Mobile ice piles up in this region because of the shape
573 of the eastward protruding coastline relative to the generally northward-flowing current.

574 There is only one short section of this transect where the fast ice was level and where we
575 clearly identified an SIPL with a thickness larger than the uncertainty of ± 0.5 m. This was in
576 Moubray Bay, where approx. 4 km of transited level ice at L in Figs. 8a&b showed an SIPL
577 which decreased in thickness from 3.3 m at the coastal end of the transect close to the floating
578 Ironside Glacier, to 1.6 m at the furthest edge of the level ice.

579

580 **5 Discussion**

581

582 5.1 Factors influencing fast ice thickness in the western Ross Sea

583

584 The region with the greatest climatological rate of decrease in fast ice extent in the
585 Southern Ocean, over 2000-2018, is Victoria & Oates Land (Fraser et al., 2021). While we are
586 unable to identify the processes causing this maximal decrease in fast ice extent, we do provide
587 baseline fast ice thicknesses for, e.g., further modeling studies, and attribute factors causing
588 thickness variations in 2017. Our AEM survey flights took place within this region between 8-13
589 November 2017 (DOY=312-317). This is 30 days later than the maximum in fast ice extent
590 (DOY=285), and therefore likely to be close to the maximum annual fast ice thickness. Along
591 the Victoria Land Coast, the fast ice is influenced by polynya processes and by Ice Shelf Water
592 generated from interaction with continental ice. Our measurements are only a snapshot in time,
593 but the processes which determine the fast ice thickness recur: that is, multiple polynya events
594 take place every year (Dale et al., 2017; Dai et al., 2020) while ISW is pervasive from year to
595 year (e.g., Budillon and Spiezie, 2000; Langhorne et al., 2015). Thus, our aim in this study is to
596 quantify the relative influence on fast ice thickness of thermodynamic growth (sometimes in the
597 presence of ISW), and of ice deformation (often caused by related polynya activity).

598 Our survey is approximately north-south covering a latitudinal gradient of just under 6
599 degrees of latitude (-77.7° to -72.0° ; approximately 650 km). While thermodynamically one
600 could expect thinner ice farther to the north, we show that, on average, the thickest fast ice, and
601 significantly thicker than the surveyed pack ice (see Rack et al. (2021) and Fig. 4b), is along the
602 northern coastal transect (see Fig. 8) from Cape Washington to Cape Adare. We have shown that
603 this is the result of deformation against coastal features, so begin by examining this deformed
604 ice.

605 5.2 Thickness of rough fast ice

606

607 Rough ice constituted 41% of the total fast ice transect length but 50% of its volume. The
608 effect of rough ice is seen in the histogram of 100-point median-filtered, in-phase, apparent
609 thickness for 2017, shown in Fig. 1. The overall result is that, while the modal ice thickness was
610 2.0 m, the mean of 2.6 ± 1.0 m was higher because of the significant contribution of rough ice to
611 the profiles. In comparison with other years, airborne and satellite altimetry implies that the
612 freeboard of the coastal sea ice of the western Ross Sea in 2017 was greater (and hence the sea

613 ice thicker) than in 2003-2008, and 2016 (Tian et al., 2021). Noting evidence that the TNB
614 polynya was also more active in 2017 than in the early 2000s (Yoon et al, 2020), we conjecture
615 that the fast ice of 2017 may have been thicker because of the multiple polynya events that sculpt
616 the fast ice edge and cause deformation against coastal features.

617 A correlation between ice thickness and surface roughness has been observed over Arctic
618 fast ice (Beckers et al., 2017). In Antarctic fast ice, Giles et al (2008) have previously highlighted
619 the contribution of rough ice to the thickness distribution. They classified fast ice in East
620 Antarctica as “smooth” or “rough”, based on calibrated radar backscatter images, and found a 2:1
621 area ratio of smooth to rough fast ice. With the definition of roughness in section 3.3, our study
622 finds a larger portion of rough ice by length, 3:2, in the western Ross Sea. Further Giles et al.
623 (2008) assigned thicknesses to “smooth” and “rough” fast ice, respectively of 1.7 m and 5.0 m.
624 The mean thicknesses measured in the western Ross Sea in spring are bracketed by these
625 extremes, with 2.0 m for level, and 3.2 m for rough respectively. We are unable to make further
626 comparison because the rough ice threshold cannot be extended beyond our 1-D survey lines to
627 provide areal information.

628 As discussed in section 4.2.4, one of the longer stretches of rough ice in our survey,
629 between locations D and F of Fig. 8a&b (from the Aviator Glacier to the Borchevink Glacier),
630 displayed thicknesses in the range 3 to 5 m (see 100 to 200 km of transect of Fig. 8b). This
631 coastline was ice free on 17 Feb 2017, but patches of mobile ice persisted offshore. As shown by
632 Rack et al. (2021), polynya activity in Terra Nova Bay drives ice eastward from the coast, that
633 then drifts north to be trapped and frozen in place against the eastward projection of the coast. It
634 is possible that thick, multiyear ice floes had become frozen within the fast ice cover. The
635 thickest ice of the survey is the rough ice from H and M of Fig. 8a&b, from north of Coulman
636 Island up to Moubray Bay (see 250 to 400 km of transect of Fig. 8b). Again this ice has been
637 attached to the coast for less than a year, but may be a mélange of thick, old floes.

638 In order to reliably identify the SIPL, we smoothed the AEM data in this work (as
639 described in section 3.2). However, over rough ice, smoothing resulted in reductions of
640 maximum ridge thicknesses which can be seen by comparing smoothed (Fig. 4a, Table 1) versus
641 unsmoothed (Fig. 4b, Table 2) fast ice statistics. While the overall mean and median values differ
642 by 0.1 m or less between smoothed and unsmoothed data, the mean value of the thickest 10% of
643 fast ice (h_{H10}) is 0.8 m thicker when unsmoothed than when smoothed. Thus we have
644 underestimated the thickest fast ice by up to 20% because of our need to smooth the data for
645 SIPL detection. In addition, it is well known that the retrieved unsmoothed thickness of
646 unconsolidated ridges may be up to 50% less than the “true” thickness (e.g., Pfaffling
647 et al., 2007; Haas & Jochmann, 2003) because of the footprint of the EM instrument. We
648 conclude that the values reported here of thickest rough fast ice may be only 40% of its “true”
649 thickness.

650

651 5.3 Volume and influence of the sub-ice platelet layer under level fast ice

652

653 In order to obtain an overall sense of the contribution of SIPL to the volume of level fast
654 ice, we consider the transect volume of SIPL in comparison to that of consolidated ice plus snow.
655 South of 75°, in New Harbour and Granite Harbour where level ice comprises 76% of the
656 transect volume, the SIPL transect bulk volume is 0.30 times consolidated ice volume, a

657 significant contribution. North of 75°, where only 33% of the volume of the fast ice is level ice,
658 the contribution of the SIPL is 0.25 times consolidated level ice volume, and thus a small
659 fraction of the total volume of ice surveyed to the north of 75°. This emphasises the dominance
660 of the McMurdo/Ross Ice Shelf in modifying sea ice in the southern Ross Sea. We caution that
661 our observations are biased by the challenges of detecting an SIPL under rougher ice using
662 airborne single-frequency EM techniques (which underestimates SIPL volume), and by the fact
663 that there is a large uncertainty in SIPL thickness, as outlined in section 3.2.

664 In spite of the caveats on our observations, ISW is clearly a factor of influence for New
665 Harbour, with 45% of the level ice surveyed having an SIPL greater than 0.5 m. We note that the
666 New Harbour transects close to locations E, G and I (Fig. 5), are in a region where Fraser et al.
667 (2021) has identified fast ice with a mean age of 18-24 months. Indeed second year ice was
668 observed there in 2017 (Fig. 5c) with a thickness of 3-5, hinting that the presence of an SIPL
669 may strongly contribute to the thickness and persistence of the fast ice at this location.

670 There is one exceptional instance of the influence of ISW; in front of the Hells Gate Ice
671 Shelf where we estimate the heat fluxes associated with the formation of level ice within 3 km of
672 the front of the ice shelf. Our results (Section 4.2.2) show that relatively thin, level ice with a
673 mean thickness of 1.1 ± 0.3 m, underlain by a substantial SIPL of thickness 3.4 ± 2.2 m (Figs.
674 6b&c), formed in 45 days, i.e. with a growth rate of 2.5 cm d^{-1} . For comparison, Purdie et al.
675 (2006) measured an average growth rate of 1.5 cm d^{-1} in a protected, supercooled bay, some 325
676 km to the south. We know that, within 5-10 days of the initial formation of the Hells Gate level
677 ice, it became sheltered by the triangular-shaped region of rough ice (Zhai et al, 2019). Held in
678 position, we assume that katabatic winds kept the sea ice surface largely free of snow (supported
679 by the photos in Fig. 3), allowing rapid heat transfer to the atmosphere. Heat transfer also took
680 place to the ocean.

681 We note that sea ice in front of the Hells Gate Ice Shelf in 2017 was of similar thickness
682 to that sampled in 1994/1995, and crystallographic evidence suggests that granular/platelet ice
683 formed throughout the entire sea ice cover (Tison et al., 1998). We therefore conjecture that,
684 over 45 days, heat has been extracted to the ocean to form 4.5 m SIPL, and that 1.1 m of this
685 SIPL became consolidated due to heat flux to the atmosphere. Assuming the SIPL has a solid
686 fraction of 0.25 (Hoppmann et al., 2020), we follow Langhorne et al. (2015) to estimate an
687 average oceanic heat flux of -90 Wm^{-2} , during October and within 3 km of the ice shelf front.
688 This value is reasonable for an October average, when the surface ocean of the western Ross Sea
689 is at its coldest (Mahoney et al., 2011), and at such close proximity to the ice shelf. The heat flux
690 to the atmosphere to consolidate the ice cover (i.e. to form 0.75×1.1 m of sea ice) requires an
691 average of 65 Wm^{-2} . This is a realistic value (Gough et al., 2012) for fast ice less than 1 m thick
692 with a thin snow cover in an area where there are frequent katabatic wind events driving high
693 turbulent heat fluxes (Tison et al., 1998).

694 The large volumes of SIPL discussed above are perhaps surprising, so can we justify
695 these? Partly they are a result of flight track limitations, and the focus on the harbour regions,
696 rather than an attempt to conduct an inclusive, representative grid survey that sampled the fast
697 ice types proportionately. Theoretical considerations (Wongpan et al., 2021) have demonstrated
698 that an SIPL grows more rapidly than congelation ice. Its growth rate is linearly related to
699 thermal forcing (as observed by e.g., Smith et al., 2012), rather than a growth rate that decreases
700 with ice thickness as for congelation ice. Thus thick SIPLs may flourish under thick fast ice,
701 explaining the large SIPL thicknesses observed (e.g., Hughes et al., 2014; Hoppmann et al.,

702 2020) and the relatively high SIPL volumes indicated here. The large liquid fraction of the SIPL
703 enhances its stability, in particular by providing a low thermal diffusivity, while convection
704 within the isothermal SIPL does not transport heat. Thus in spite of the fact that an SIPL
705 provides little extra mechanical strength to the sea ice cover, its thermal properties isolate the
706 base of the sea ice from the ocean below. Since our knowledge of the SIPL is very poor during
707 the decay period (Wongpan et al., 2021), the amount of extra protection provided by an SIPL to
708 the fast ice that fringes continental ice is a key topic of future study.

709 **6 Conclusions**

710 As a baseline for future studies, this first-time inventory of fast ice thickness in the
711 western Ross Sea is the result of a 700 km long airborne electromagnetic (AEM) induction
712 survey in November 2017 over mainly first-year fast ice. The thickness of a sub-ice platelet layer
713 (SIPL) can be estimated under level ice, but not under rough ice, incentivising the use of a
714 level/rough ice filter. The AEM flights took place approximately 30 days after the maximum in
715 fast ice extent in Victoria & Oates Land, and it is therefore likely that the fast ice was close to its
716 maximum annual thickness. Only in New Harbour had the ice been in place throughout the
717 previous summer. In the following we address the three questions posed at the end of the
718 Introduction (section 1).

719 (i) For the fast ice of the Victoria Land coast between New Harbour and Cape Adare, the
720 modal consolidated ice (+ snow) thickness was 1.9 m, significantly less than its mean of 2.6 ± 1.0
721 m. The overall thickness distribution was a superposition of the distribution of level ice (mode =
722 2.0 m; mean = 2.0 ± 0.6 m) with rough ice (mode = 3.3 m; mean = 3.2 ± 1.2 m). The mean and
723 median of fast ice thicknesses were approx. 0.7 m (~30-40%) greater than a concurrent survey of
724 pack ice in the same region (Rack et al., 2021), while the mode was more than 1.5 m greater in
725 the fast ice. Thus while the area covered by land-fast sea ice was only 2% of the total sea ice area
726 in the western Ross Sea in November 2017 (Li et al., 2020), the fast ice contribution to sea ice
727 volume was significant.

728 (ii) The fast ice of the western Ross Sea consists of significant proportions (41% by
729 transect length, 50% by transect volume) of rough ice. Deformation is closely linked with
730 polynya activity and multiple such events occur every year, sculpting the fast ice edge. While the
731 modal thicknesses of thermodynamically-grown, level ice north of 75°S was 0.1 m thinner than
732 that south of 75°S, overall the northern ice was 0.4 m thicker (2.8 m versus 2.4 m) on average
733 because of the higher proportion of rough ice in the north (58% versus 19% by transect length).
734 On average the thickest fast ice lay along the coast from Cape Washington to Cape Adare. This
735 demonstrates that any effect of latitudinal gradient in climate, snow cover, or the presence of
736 ISW, is overwhelmed by ice deformation against coastal features. The thickest 10% of rough fast
737 ice had a mean of almost 6 m, and in Moubray Bay a 2 km long stretch was observed with a
738 thickness in excess of 8 m.

739 (iii) The presence of an SIPL, likely due to ISW in the upper surface ocean, was
740 definitively observed in four embayments: the Silverfish Bay region of Terra Nova Bay, offshore
741 Hells Gate Ice Shelf, New Harbour, and Granite Harbour. Beneath level fast ice an SIPL with a
742 mean of 0.6 ± 1.0 m, mode = 0.1 m, existed along the Victoria Land coast. This disguises the fact
743 that in some locations the SIPL was almost 10 m thick, and the thickest 10% had an average
744 thickness of 2.7 m. Indeed, in New and Granite harbours the SIPL transect bulk volume was a
745 significant fraction (0.30) of the consolidated ice volume. We estimate that the sheltered fast ice

746 in front of the Hells Gate Ice Shelf formed with average heat loss to the ocean of 90 Wm^{-2} during
747 October, while simultaneous heat loss to the atmosphere implies a vigorous wind-driven
748 component. There were areas where there was a hint of an SIPL beneath level ice, such as close
749 to the Ironside Glacier front in northern Victoria Land. It is very likely that thin SIPLs are more
750 pervasive than implied from our survey because they can only be clearly detected with AEM
751 when their thickness is greater than 0.5 m, and because an SIPL cannot be detected in the
752 presence of heavily deformed ice, with unconsolidated keels, which was abundant in the study
753 region. In addition, our one-dimensional flight tracks still sparsely cover the land-fast ice.
754 Clearly proximity to continental ice, that drives katabatic winds and generates ISW, is a critical
755 factor for the thickness Antarctic fast ice.

756

757 **Acknowledgments**

758 This project was funded by the NZ Deep South National Science Challenge. We are very grateful
759 for the support of Antarctica NZ (event K066) and the Italian Antarctic program and the staff at
760 Scott Base and Mario Zucchelli Station. We particularly thank John Leitch and his team for
761 excellent ground support for aircraft operations. This project would not have been possible
762 without KBA BT67 crew Jamie Chisholm, Aaron Neyrinck, and Jan Verburg. The AEM
763 equipment used in this study was developed with grants from the Alberta Ingenuity and the
764 Canada Research Chairs programmes to CH.

765

766 **Data Availability**

767 The airborne electromagnetic induction data collected in the western Ross Sea in the study are
768 under review at PANGAEA, Data submission ticket PDI-32716.

769

770 **References**

771 Ainley, D.G., Larue, M.A., Stirling, I., Stammerjohn, S. & Siniff, D.B. (2015). An apparent
772 population decrease, or change in distribution, of Weddell seals along the Victoria Land coast.
773 *Mar Mam Sci*, 31, 1338-1361. <https://doi.org/10.1111/mms.12220>

774

775 Arndt, S., Hoppmann, M., Schmithüsen, H., Fraser, A. D., & Nicolaus, M. (2020). Seasonal and
776 interannual variability of landfast sea ice in Atka Bay, Weddell Sea, Antarctica, *The Cryosphere*,
777 14, 2775–2793. <https://doi.org/10.5194/tc-14-2775-2020>.

778

779 Barry, J. P. (1988). Hydrographic patterns in McMurdo Sound, Antarctica and their relationship
780 to local benthic communities, *Polar Biol.*, 8(5), 377–391. <https://doi:10.1007/BF00442029>.

781 Beckers, J., Renner, A., Spreen, G., Gerland, S., & Haas, C. (2015). Sea-ice surface roughness
782 estimates from airborne laser scanner and laser altimeter observations in Fram Strait and north of
783 Svalbard. *Annals of Glaciology*, 56(69), 235-244. <https://doi:10.3189/2015AoG69A717>

- 784
785 Bell, R., Chu, W., Kingslake, J. *et al.* (2017). Antarctic ice shelf potentially stabilized by export
786 of meltwater in surface river. *Nature* 544, 344–348 <https://doi.org/10.1038/nature22048>
787
- 788 Brett G. M., Irvin A., Rack W., Haas C., Langhorne P. J., & Leonard, G. H. (2020). Variability
789 in the distribution of fast ice and the sub-ice platelet layer near McMurdo Ice Shelf. *Journal of*
790 *Geophysical Research: Oceans*. doi: 10.1029/2019JC015678.
791
- 792 Brett, G. M., Price, D., Rack, W., & Langhorne, P. J. (2021). Satellite altimetry detection of ice-
793 shelf-influenced fast ice, *The Cryosphere*, 15, 4099–4115. [https://doi.org/10.5194/tc-15-4099-](https://doi.org/10.5194/tc-15-4099-2021)
794 2021.
795
- 796 Budillon, G. & Spezie, G. (2000). Thermohaline structure and variability in the Terra Nova Bay
797 polynya, Ross Sea, *Antarct. Sci.*, 12, 493–508, <https://doi.org/10.1017/S0954102000000572>
798
- 799 Cummings, V.J., Barr, N.G., Budd, R.G. *et al.* (2019). *In situ* response of Antarctic under-ice
800 primary producers to experimentally altered pH. *Sci Rep* 9, 6069.
801 <https://doi.org/10.1038/s41598-019-42329-0>
802
- 803 Currie, A. A., Marshall A. J., Lohrer A. M., Cummings V. J., Seabrook S., & Cary S. C. (2021).
804 Sea Ice Dynamics Drive Benthic Microbial Communities in McMurdo Sound, Antarctica. *Front.*
805 *Microbiol.*, 12. <https://doi.org/10.3389/fmicb.2021.745915>
806
- 807 Dai L, Xie H, Ackley SF, Mestas-Nuñez AM. (2020). Ice Production in Ross Ice Shelf Polynyas
808 during 2017–2018 from Sentinel–1 SAR Images. *Remote Sensing*. 12(9),1484.
809 <https://doi.org/10.3390/rs12091484>
810
- 811 Dale, E. R., McDonald, A. J., Coggins, J. H. J., and Rack, W. (2017). Atmospheric forcing of sea
812 ice anomalies in the Ross Sea polynya region, *The Cryosphere*, 11, 267–280,
813 <https://doi.org/10.5194/tc-11-267-2017>.
814
- 815 Debenham, F. (1965). The Glacier Tongues of McMurdo Sound. *The Geographical Journal*
816 131(3), 369–71. <https://doi.org/10.2307/1794191>.
817
- 818 Foldvik, A., & Kvinge, T. (1974). Conditional instability of sea-water at freezing-point, *Deep*
819 *Sea Res.*, 21(3), 69–174. doi:10.1016/0011-7471(74)90056-4.
820
- 821 Foley, N., Tulaczyk, S.M., Grombacher D, Doran PT, Mikucki J, Myers KF, Foged N, Dugan H,
822 Auken E, & Virginia R. (2019). Evidence for Pathways of Concentrated Submarine Groundwater
823 Discharge in East Antarctica from Helicopter-Borne Electrical Resistivity Measurements.
824 *Hydrology*, 6(2), 54. <https://doi.org/10.3390/hydrology6020054>
825
- 826 Fons, S. W., & Kurtz, N. T. (2019). Retrieval of snow freeboard of Antarctic sea ice using
827 waveform fitting of CryoSat-2 returns. *The Cryosphere*, 13, 861–878. [https://doi.org/10.5194/tc-](https://doi.org/10.5194/tc-13-861-2019)
828 13-861-2019
829

- 830 Fraser, A. D., Massom, R. A., Ohshima, K. I., Willmes, S., Kappes, P. J., Cartwright, J., &
831 Porter-Smith, R. (2020). High-resolution mapping of circum-Antarctic landfast sea ice
832 distribution, 2000–2018. *Earth Syst. Sci. Data*, *12*, 2987–2999, [https://doi.org/10.5194/essd-12-](https://doi.org/10.5194/essd-12-2987-2020)
833 [2987-2020](https://doi.org/10.5194/essd-12-2987-2020).
- 834
835 Fraser, A. D., Massom, R. A., Handcock, M. S., Reid, P., Ohshima, K. I., Raphael, M. N.,
836 Cartwright, J., Klekociuk, A. R., Wang, Z., & Porter-Smith, R. (2021). 18 year record of circum-
837 Antarctic landfast sea ice distribution allows detailed baseline characterisation, reveals trends
838 and variability. *The Cryosphere*, *15*, 5061–5077. <https://doi.org/10.5194/tc-15-5061-2021>
839
- 840 Frezzotti, M. (1997). Ice front fluctuation, iceberg calving flux and mass balance of Victoria
841 Land glaciers. *Antarctic Science*, *9*(1), 61-73. doi:10.1017/S0954102097000096
842
- 843 Fusco, G., Budillon, G., & Spezie, G. (2009). Surface heat fluxes and thermohaline variability in
844 the Ross Sea and in Terra Nova Bay polynya. *Cont. Shelf Res.*, *29*, 1887–1895,
845 <https://doi.org/10.1016/j.csr.2009.07.006>.
- 846 Giles, A. B., Massom, R. A. & Lytle V. I. (2008). Fast-ice distribution in East Antarctica during
847 1997 and 1999 determined using RADARSAT data, *J. Geophys. Res.*, *113*, C02S14.
848 doi:10.1029/2007JC004139.
- 849 Gomez-Fell, R., Rack, W., Purdie, H., & Marsh, O. (2022). Parker Ice Tongue collapse,
850 Antarctica, triggered by loss of stabilizing land-fast sea ice. *Geophysical Research Letters*, *49*,
851 e2021GL096156. <https://doi.org/10.1029/2021GL096156>
852
- 853 Gough, A., Mahoney, A., Langhorne, P., Williams, M., Robinson, N., & Haskell, T. (2012).
854 Signatures of supercooling: McMurdo Sound platelet ice. *Journal of Glaciology*, *58*(207), 38-50.
855 doi:10.3189/2012JoG10J218
856
- 857 Gow, A. J., Ackley, S. F., Govoni, J. W. & Weeks, W. F. (1998). Physical and structural
858 properties of land-fast sea ice in McMurdo Sound, Antarctica, in *Antarctic Sea Ice: Physical*
859 *Processes, Interactions and Variability*, *Antarct. Res. Ser.*, vol. 74, edited by M. O. Jeffries, pp.
860 355–374, AGU, Washington, D. C., doi:10.1029/AR074p0355.
861
- 862 Haas, C. (2004). Airborne EM sea-ice thickness profiling over brackish Baltic sea water,
863 Proceedings of the 17th international IAHR symposium on ice, June 21-25, 2004, St. Petersburg,
864 Russia, All-Russian Research Institute of Hydraulic Engineering (VNIIG), Saint Petersburg,
865 Russia, 2, 12-17.
866
- 867 Haas, C. (2006). Airborne electromagnetic sea ice thickness sounding in shallow, brackish water
868 environments of the Caspian and Baltic Seas, Proceedings of OMAE2006 25th International
869 Conference on Offshore Mechanics and Arctic Engineering, June 4-9, 2006, Hamburg, Germany.
870
- 871 Haas, C., Hendricks, S., Eicken, H., & Herber, A. (2010). Synoptic airborne thickness surveys
872 reveal state of Arctic sea ice cover. *Geophysical Research Letters*, *37*, L09501.
873 <https://doi.org/10.1029/2010GL042652>

- 874
875 Haas, C., & Jochmann, P. (2003). Continuous EM and ULS thickness profiling in support of ice
876 force measurements. In *Proceedings of the 17th International Conference on Port and Ocean*
877 *engineering under Arctic Conditions POAC '03* (pp. 849–856). Trondheim, Norway. June 16–19,
878 2003.
- 879
880 Haas, C., Langhorne, P. J., Rack, W., Leonard, G. H., Brett, G. M., Price, D., Beckers, J. F., &
881 Gough, A. J. (2021). Airborne mapping of the sub-ice platelet layer under fast ice in McMurdo
882 Sound, Antarctica, *The Cryosphere*, 15, 247–264. <https://doi.org/10.5194/tc-15-247-2021>.
- 883
884 Haas, C., Lobach, J., Hendricks, S., Rabenstein, L., & Pfaffling, A. (2009). Helicopter-borne
885 measurements of sea ice thickness, using a small and lightweight, digital EM system. *Journal of*
886 *Applied Geophysics*, 67(3), 234–241. <https://doi.org/10.1016/j.jappgeo.2008.05.005>
- 887
888 Han, H., & Lee, H. (2018). Glacial and tidal strain of landfast sea ice in Terra Nova Bay, East
889 Antarctica, observed by interferometric SAR techniques, *Remote Sensing of Environment*, 209,
890 41–51. <https://doi.org/10.1016/j.rse.2018.02.033>.
- 891
892 Han, H., Kim S. H., & Kim S. (2022). Decadal changes of Campbell Glacier Tongue in East
893 Antarctica from 2010 to 2020 and implications of ice pinning conditions analyzed by optical and
894 SAR datasets, *GIScience & Remote Sensing*, 59(1), 705–721.
895 <https://doi.org/10.1080/15481603.2022.2055380>
- 896
897 Hellmer, H. H. (2004). Impact of Antarctic ice shelf basal melting on sea ice and deep ocean
898 properties, *Geophys. Res. Lett.*, 31, L10307. doi:10.1029/2004GL019506.
- 899
900 Hollands, T., & Dierking, W. (2016). Dynamics of the Terra Nova Bay polynya: The potential of
901 multi-sensor observations. *Remote Sensing of Environment*, 187, 30–48.
902 <https://doi.org/10.1016/j.rse.2016.10.003>
- 903
904 Hoppmann, M., Richter, M., Smith, I., Jendersie, S., Langhorne, P., Thomas, D., & Dieckmann,
905 G. (2020). Platelet ice, the Southern Ocean's hidden ice: A review. *Annals of Glaciology*, 1–28.
doi:10.1017/aog.2020.54
- 906
907 Hughes, K. G., Langhorne, P. J., Leonard, G. H., & Stevens C. L. (2014). Extension of an Ice
908 Shelf Water plume model beneath sea ice with application in McMurdo Sound, Antarctica, *J.*
Geophys. Res. Oceans, 119. doi:10.1002/2013JC009411.
- 909
910 Hunkeler, P. A., Hoppmann, M., Hendricks, S., Kalscheuer, T., & Gerdes, R. (2015). A glimpse
911 beneath Antarctic sea ice: Platelet layer volume from multifrequency electromagnetic induction
sounding, *Geophys. Res. Lett.*, 43, 222–231. <https://doi.org/10.1002/2015GL065074>.
- 912
913 Jacobs, S. S., Fairbanks, R. G., & Horibe Y. (1985). Origin and evolution of water masses near
914 the Antarctic continental margin: Evidence from H¹⁸O/H¹⁶O ratios in seawater, in *Oceanology of*
the Antarctic Continental Shelf, edited by S. S. Jacobs, AGU, Washington, D. C., 22
915 doi:10.1029/AR043p0059.

- 916
917 Jeffries, M. O., Weeks, W. F., Shaw, R., & Morris, K. (1993). Structural characteristics of
918 congelation and platelet ice and their role in the development of Antarctic land-fast sea ice, *J.*
919 *Glaciol.*, *39*(132), 223–238.
- 920 Jendersie, S., Williams, M. J. M., Langhorne, P. J., & Robertson, R. (2018). The density-driven
921 winter intensification of the Ross Sea circulation, *J. Geophys. Res.-Oceans*, *123*, 1–23,
922 <https://doi.org/10.1029/2018JC013965>.
- 923 Jenouvrier, S., Che-Castaldo, J., Wolf, S., Holland, M., Labrousse, S., LaRue, M., Wienecke, B.,
924 Fretwell, P., Barbraud, C., Greenwald, N., Stroeve, J., & Trathan, P. N. (2021). The call of the
925 emperor penguin: Legal responses to species threatened by climate change. *Global Change*
926 *Biology*, *27*, 5008– 5029. <https://doi.org/10.1111/gcb.15806>
927
- 928 Kacimi, S. and Kwok, R. (2020). The Antarctic sea ice cover from ICESat-2 and CryoSat-2:
929 freeboard, snow depth, and ice thickness, *The Cryosphere*, *14*, 4453–4474.
930 <https://doi.org/10.5194/tc-14-4453-2020>.
- 931
932 Kusahara, K., & Hasumi H. (2014). Pathways of basal meltwater from Antarctic ice shelves: a
933 model study. *Journal of Geophysical Research-Oceans*, *119*, 5690-5704.
934 <https://doi.org/10.1002/2014JC009915>
935
- 936 Langhorne, P. J., Hughes, K. G., Gough, A. J., Smith, I. J., Williams, M. J. M., Robinson, N. J.,
937 Stevens, C. L., Rack, W., Price, D., Leonard, G. H., Mahoney, A. R., Haas, C., & Haskell, T. G.
938 (2015). Observed platelet ice distributions in Antarctic sea ice: An index for ocean-ice shelf heat
939 flux. *Geophys. Res. Lett.*, *42*, 5442–5451. doi:10.1002/2015GL064508.
940
- 941 Leonard, G. H., Purdie, C. R., Langhorne, P. J., Haskell, T. G., Williams, M. J. M., & Frew R. D.
942 (2006). Observations of platelet ice growth and oceanographic conditions during the winter of
943 2003 in McMurdo Sound, Antarctica, *J. Geophys. Res.*, *111*, C04012.
944 doi:10.1029/2005JCC002952.
945
- 946 Leonard, G. H., Turner, K. E., Richter, M. E., Whittaker, M. S., & Smith, I. J. (2021). Brief
947 communication: The anomalous winter 2019 sea-ice conditions in McMurdo Sound, Antarctica,
948 *The Cryosphere*, *15*, 4999–5006. <https://doi.org/10.5194/tc-15-4999-2021>.
949
- 950 Lewis, E. L., & Perkin R. G. (1985). The winter oceanography of McMurdo Sound, Antarctica,
951 in *Oceanology of the Antarctic Continental Shelf*, *Antarct. Res. Ser.*, edited by S. S. Jacobs, pp.
952 145–165, AGU, Washington, D. C.
953
- 954 Li, X., Shokr, M., Hui, F., Chi, Z., Heil, P., Chen, Z., Yu, Y., Zhai, M., & Cheng, X. (2020). The
955 spatio-temporal patterns of landfast ice in Antarctica during 2006–2011 and 2016–2017 using
956 high- resolution SAR imagery, *Remote Sens. Environ.*, *242*, 111736.
957 <https://doi.org/10.1016/j.rse.2020.111736>.

- 958 Mager, S. M., Smith, I. J., Kempema, E. W., Thomson, B. J., & Leonard G. H. (2013). Anchor
959 ice in polar oceans. *Progress in Physical Geography: Earth and Environment*, 37(4), 468-483.
960 doi:10.1177/0309133313479815
- 961
- 962 Mahoney, A. R., Gough, A. J., Langhorne, P. J., Robinson, N. J., Stevens, C. L., Williams, M. J.
963 M. & Haskell, T. G. (2011). The seasonal appearance of ice shelf water in coastal Antarctica and
964 its effect on sea ice growth, *J. Geophys. Res.*, 116, C11032. doi:10.1029/2011JC007060.
- 965
- 966 Massom, R., Hill, K., Lytle, V., Worby, A., Paget, M., & Allison, I. (2001). Effects of regional
967 fast-ice and iceberg distributions on the behaviour of the Mertz Glacier polynya, East
968 Antarctica. *Annals of Glaciology*, 33, 391-398. doi:10.3189/172756401781818518
- 969
- 970 Massom, R.A., Scambos, T.A., Bennetts, L.G., Reid, P., Squire, V.A. and Stammerjohn, S.E.
971 (2018). Antarctic ice shelf disintegration triggered by sea ice loss and ocean swell. *Nature*, 558,
972 383–389. <https://doi.org/10.1038/s41586-018-0212-1>
- 973
- 974 McPhee, M. G., Stevens, C. L., Smith, I. J., & Robinson, N. J. (2016). Turbulent heat transfer as
975 a control of platelet ice growth in supercooled under-ice ocean boundary layers. *Ocean Science*,
976 12 (2), 507–515. doi: 10.5194/os-12-507-2016
- 977
- 978 Meiners, K. M., Vancoppenolle, M., Carnat, G., Castellani, G., Delille, B., Delille, D., et al.
979 (2018). Chlorophyll-a in Antarctic landfast sea ice: A first synthesis of historical ice core data.
980 *Journal of Geophysical Research: Oceans*, 123, 8444–8459. [https://doi.org/](https://doi.org/10.1029/2018JC014245)
981 10.1029/2018JC014245
- 982
- 983 Mezgec, K., Stenni, B., Crosta, X. *et al.* (2017). Holocene sea ice variability driven by wind and
984 polynya efficiency in the Ross Sea. *Nat Commun*, 8, 1334. [https://doi.org/10.1038/s41467-017-](https://doi.org/10.1038/s41467-017-01455-x)
985 01455-x
- 986
- 987 Moreçki, V. N. (1965). Underwater sea ice, *Probl. Arkt. Antarkt.*, 19, 32–38. English translation
988 by E. R. Hope, DRB Canada Report No. T497R April, 1968.
- 989
- 990 Murray, K.T., Miller, M.F. & Bowser, S.S. (2013). Depositional processes beneath coastal multi-
991 year sea ice. *Sedimentology*, 60, 391-410. <https://doi.org/10.1111/j.1365-3091.2012.01345.x>
- 992
- 993 Nakata, K., Ohshima, K. I., & Nihashi, S. (2021). Mapping of active frazil for Antarctic coastal
994 polynyas, with an estimation of sea-ice production. *Geophysical Research Letters*, 48,
995 e2020GL091353. <https://doi.org/10.1029/2020GL091353>
- 996
- 997 Nihashi, S., & Ohshima, K. I. (2015). Circumpolar Mapping of Antarctic Coastal Polynyas and
998 Landfast Sea Ice: Relationship and Variability, *Journal of Climate*, 28(9), 3650-3670.
999 10.1175/JCLI-D-14-00369.1
- 1000
- 1001 Pfaffling, A., Haas, C., & Reid, J. E. (2007). Direct helicopter EM—Sea-ice thickness inversion
1002 assessed with synthetic and field data. *Geo- physics*, 72(4), F127–F137.
1003 <https://doi.org/10.1190/1.2732551>

- 1004
1005 Price, D., Rack, W., Haas, C., Langhorne, P. J. & Marsh O. (2013). Sea ice freeboard in
1006 McMurdo Sound, Antarctica, derived by surface-validated ICESat laser altimeter data, *J.*
1007 *Geophys. Res. Oceans*, 118. <https://doi.org/10.1002/jgrc.20266>.
1008
- 1009 Price, D., Rack, W., Langhorne, P. J., Haas, C., Leonard G.H. & Barnsdale K. (2014). The sub-
1010 ice platelet layer and its influence on freeboard to thickness conversion of Antarctic sea ice. *The*
1011 *Cryosphere*, 8, 1031-1039. <https://doi.org/10.5194/tc-8-1031-2014>.
1012
- 1013 Price, D., Beckers, J., Ricker, R., Kurtz, N., Rack, W., Haas, C., Helm, V., Hendricks, S.
1014 Leonard, G. & Langhorne, P. J. (2015). Evaluation of CryoSat-2 derived sea ice freeboard over
1015 fast ice in McMurdo Sound, Antarctica. *Journal of Glaciology*. 61(226),
1016 <https://doi.org/10.3189/2015JoG14J157>.
1017
- 1018 Price, D., Soltanzadeh, I., Rack, W., & Dale, E. (2019). Snow-driven uncertainty in CryoSat-2-
1019 derived Antarctic sea ice thickness – insights from McMurdo Sound, *The Cryosphere*, 13, 1409–
1020 1422. <https://doi.org/10.5194/tc-13-1409-2019>.
1021
- 1022 Purdie, C., Langhorne, P., Leonard, G., & Haskell, T. (2006). Growth of first-year landfast
1023 Antarctic sea ice determined from winter temperature measurements. *Annals of Glaciology*, 44,
1024 170-176. doi:10.3189/172756406781811853
1025
- 1026 Rabenstein, L., Hendricks, S., Martin, T., Pfaffhuber, A. & Haas, C. (2010). Thickness and
1027 surface-properties of different sea-ice regimes within the Arctic Trans Polar Drift: Data from
1028 summers 2001, 2004 and 2007, *J. Geophys. Res.*, 115, C12059. doi:10.1029/2009JC005846.
1029
- 1030 Rack, W., Haas, C. & Langhorne, P. J. (2013). Airborne thickness and freeboard measurements
1031 over the McMurdo Ice Shelf, Antarctica, and implications for ice density, *J. Geophys. Res.*
1032 *Oceans*, 118, doi:10.1002/2013JC009084.
1033
- 1034 Rack, W., Price, D., Haas, C., Langhorne, P. J., & Leonard, G. H. (2021). Sea ice thickness in
1035 the Western Ross Sea. *Geophysical Research Letters*, 48, e2020GL090866.
1036 <https://doi.org/10.1029/2020GL090866>
1037
- 1038 Robinson, N. J., Williams, M. J. M., Stevens, C. L., Langhorne, P. J., & Haskell, T. G. (2014).
1039 Evolution of a supercooled Ice Shelf Water plume with an actively-growing sub-ice platelet
1040 matrix. *J. Geophys. Res. Oceans*, 119(6), 3425-3446. doi: 10.1002/2013JC009399.
1041
- 1042 Rossiter, J. R. & Holladay, J. S. (1994). Ice-thickness measurement. In *Remote Sensing of Sea*
1043 *Ice and Icebergs*, Haykin, S., Lewis, E. O., Rainey, R. K., and Rossiter, J. R. (Eds.), John Wiley
1044 and Sons Inc., New York, NY, 141–176.
1045
- 1046 Smith, I. J., Langhorne, P. J., Frew, R. D., Vennell, R., & Haskell, T. G. (2012). Sea ice growth
1047 rates near ice shelves. *Cold Regions Science and Technology*, 83–84, 57–70. [https://doi-](https://doi-org.ezproxy.otago.ac.nz/10.1016/j.coldregions.2012.06.005)
1048 [org.ezproxy.otago.ac.nz/10.1016/j.coldregions.2012.06.005](https://doi-org.ezproxy.otago.ac.nz/10.1016/j.coldregions.2012.06.005)
1049

- 1050 SooHoo, J.B., Palmisano, A. C., Kottmeier, S. T., Lizzotte, M. P., SooHoo S. L. & Sullivan C.
1051 W. (1987). Spectral light absorption and quantum yield of photosynthesis in sea ice microalgae
1052 and a bloom of *Phaeocystis pouchetii* from McMurdo Sound, Antarctica. *Marine Ecology*
1053 *Progress Series* 39, 175–189. doi: 10.3354/meps039175.
- 1054
1055 Souchez, R., Meneghel, M., Tison, J. L., Lorrain, R., Ronveaux, D., Baroni, C., Lozej, A.,
1056 Tobacco, I., & Jouzel, J. (1991). Ice composition evidence of marine-ice transfer along the
1057 bottom of a small Antarctic ice shelf. *Geophys Res Lett*, 18(5), 849- 852.
- 1058
1059 Stevens, C. L., Sirguey, P., Leonard, G. H., & Haskell, T. G. (2013). *Brief Communication* "The
1060 2013 Erebus Glacier Tongue calving event", *The Cryosphere*, 7, 1333–
1061 1337, <https://doi.org/10.5194/tc-7-1333-2013>.
- 1062
1063 Stevens, C. L., McPhee, M. G., Forrest, A. L., Leonard, G. H., Stanton, T., & Haskell, T. G.
1064 (2014). The influence of an Antarctic glacier tongue on near-field ocean circulation and mixing,
1065 *J. Geophys. Res. Oceans*, 119, 2344– 2362. doi:10.1002/2013JC009070.
- 1066
1067 Stevens, C., Sang Lee, W., Fusco, G., Yun, S., Grant, B., Robinson, N., & Yeon Hwang, C.
1068 (2017). The influence of the Drygalski Ice Tongue on the local ocean. *Annals of Glaciology*,
1069 58(74), 51-59. doi:10.1017/aog.2017.4
- 1070
1071 Stockton, W. (1983). Submarine Ice Cliffs on the West Side of McMurdo Sound, Antarctica.
1072 *Journal of Glaciology*, 29(102), 272-282. doi:10.3189/S0022143000008327
- 1073
1074 Tamura, T., Ohshima, K. I., Fraser, A. D. & Williams, G. D. (2016). Sea ice production
1075 variability in Antarctic coastal polynyas. *Journal of Geophysical Research*, 121, 2967-2979.
1076 doi:10.1002/2015JC011537.
- 1077
1078 Tian, L., Xie, H., Ackley, S. F., Tinto, K. J., Bell, R. E., Zappa, C. J., Gao, Y. & Mestas-Nuñez
1079 A. M. (2020). Sea Ice Freeboard in the Ross Sea from Airborne Altimetry IcePod 2016–2017
1080 and a Comparison with IceBridge 2013 and ICESat 2003–2008. *Remote Sensing*, 12(14), 2226.
1081 <https://doi.org/10.3390/rs12142226>
- 1082
1083 Tin, T., & Jeffries, M. (2001). Sea-ice thickness and roughness in the Ross Sea, Antarctica.
1084 *Annals of Glaciology*, 33, 187-193. doi:10.3189/172756401781818770
- 1085
1086 Tison, J.-L., Lorrain, R. D., Bouzette A., Dini M., Bondesan A. & Stievenard M. (1998). Linking
1087 landfast sea ice variability to marine ice accretion at Hells Gate Ice Shelf, Ross Sea. In *Antarctic*
1088 *sea ice: physical processes, interactions and variability*. American Geophysical Union,
1089 Washington, DC, 375–407.
- 1090
1091 Vacchi, M., DeVries, A.L., Evans, C.W. *et al.* (2012). A nursery area for the Antarctic silverfish
1092 *Pleuragramma antarcticum* at Terra Nova Bay (Ross Sea): first estimate of distribution and
1093 abundance of eggs and larvae under the seasonal sea-ice. *Polar Biol*, 35, 1573–1585.
1094 <https://doi.org/10.1007/s00300-012-1199-y>
- 1095

- 1096 Van Woert, M., Meier, W., Zou, C., Archer, A., Pellegrini, A., Grigioni, P., & Bertoina, C.
1097 (2001). Satellite observations of upper-ocean currents in Terra Nova Bay, Antarctica. *Annals of*
1098 *Glaciology*, 33, 407-412. doi:10.3189/172756401781818879
1099
- 1100 von Albedyll, L., Haas, C., and Dierking, W. (2021). Linking sea ice deformation to ice
1101 thickness redistribution using high-resolution satellite and airborne observations, *The*
1102 *Cryosphere*, 15, 2167–2186 <https://doi.org/10.5194/tc-15-2167-2021>
1103
- 1104 Wadhams, P., & Horne, R. (1980). An Analysis Of Ice Profiles Obtained By Submarine Sonar In
1105 The Beaufort Sea. *Journal of Glaciology*, 25(93), 401-424. doi:10.3189/S0022143000015264
1106
- 1107 Wongpan, P., Vancoppenolle, M., Langhorne, P. J., Smith, I. J., Madec, G., Gough, A. J., et al.
1108 (2021). Sub-ice platelet layer physics: Insights from a mushy-layer sea ice model. *Journal of*
1109 *Geophysical Research: Oceans*, 126, e2019JC015918. <https://doi.org/10.1029/2019JC015918>
1110
- 1111 Yoon, S.-T., Lee, W. S., Stevens, C., Jendersie, S., Nam, S.H., Yun, S., Hwang, C. Y., Jang, G. I.
1112 & Lee, J. (2020). Variability in high-salinity shelf water production in the Terra Nova Bay
1113 polynya, Antarctica. *Ocean Science*, 16(2), 373. <https://doi.org/10.5194/os-16-373-2020>
1114
- 1115 Zhai, M., Zhao, T., Hui, F., Cheng, X., Liu, A., Yuan, J., Yu, Y., & Ding, Y. (2019). Anomalous
1116 extensive landfast sea ice in the vicinity of Inexpressible Island, Antarctica. *Adv. Polar Sci.*,
1117 30(4), 406–411. doi: 10.13679/j.advps.2018.0044
1118

1119 **Figure captions**

1120 **Figure 1.** In-phase apparent thickness (h_I), smoothed with 100 point median filter, for entire
 1121 coastal survey displayed on Sentinel-1 Interferometric Wide (IW) swath mode image mosaic;
 1122 images acquired between 10-20th November 2017. Level ice thickness is thicker line (squares),
 1123 rough ice is thinner line (circles). Boxes show bounds of Figs 5 (NGH), 6 (HG), 7(TNB), 8
 1124 (NVL). Survey located on Antarctic overview map (top left). Fast ice edge indicated by green
 1125 line. Histogram insert shows distribution of the level, rough and all in-phase apparent
 1126 thicknesses of fast ice within the green ice edge.

1127
 1128 **Figure 2.** Map of coastline of (a) McMurdo Sound to Granite Harbour and (b) Victoria Land
 1129 north of 75°S (cf. Fig. 1). Fast ice persistence in November taken from Fraser et al. (2020)
 1130 dataset for 2000-2018. Ice shelves and tongues shown in dark grey. Light grey pixels are the
 1131 terrestrial ice mask from Fraser et al. (2020). Fast ice edge determined by Fraser et al. (2020) for
 1132 12 November 2017 indicated by black line. AEM flight lines between 8 & 13 November 2017
 1133 shown in magenta.

1134
 1135 **Figure 3.** Illustration of identification of rough and level ice and the SIPL off the Hells Gate Ice
 1136 Shelf (on left). Thicknesses are shown downwards from snow/ice surface at 0 m, plotted against
 1137 distance from ice shelf front. In-phase and quadrature apparent thicknesses under rough (circles)
 1138 and level (squares) fast ice are compared. Unsmoothed data in grey. All other data are smoothed
 1139 with 100 point median filter. Quadrature apparent thickness (h_Q) in brown, quadrature plus SIPL
 1140 in blue (uncertainty indicated by bar), and in-phase apparent thickness (h_I) in orange. Under level
 1141 ice h_Q represents the consolidated ice thickness, while for rough ice h_I is the best measure, as
 1142 denoted by larger symbols. Photo mosaics of sea ice surface features, showing transitions from
 1143 ice shelf to nearshore level ice (cyan), from nearshore level to rough ice (grey), and from rough
 1144 to pack ice (magenta). Boundaries identified from aerial photographs (dotted) and roughness
 1145 algorithm (dashed) shown as vertical lines.

1146
 1147 **Figure 4.** (a) Probability distributions of 100-point median filtered fast ice thicknesses in
 1148 western Ross Sea in November 2017. Upper four panels show ‘south of 75°S’, lower four panels
 1149 ‘north of 75°S’. Panels show all in-phase apparent thicknesses h_I in orange, rough h_I in orange,
 1150 level h_Q in brown, and SIPL in blue. The mean (red), median (blue), mode (cyan) and h_{H10}
 1151 (magenta) bars are shown for each distribution. The number of samples (N) in each dataset is
 1152 given. (b) Probability distributions of unsmoothed in-phase apparent thicknesses (h_I) in the
 1153 western Ross Sea in November 2017, comparing fast ice with pack ice from Rack et al. (2021).
 1154 Top two panels compare all fast ice (F) with all pack ice (P) thicknesses. Fast ice (F) and pack
 1155 ice (P) data ‘south of 75°S’ and ‘north of 75°S’ are compared in the middle and bottom two
 1156 panels, respectively. The mean (red), median (blue), mode (cyan) and h_{H10} (magenta) bars are
 1157 shown for each distribution. The number of samples (N) in each dataset is given.

1158
 1159 **Figure 5.** New Harbour and Granite Harbour. (a) In-phase apparent thickness (h_I) plotted on
 1160 Sentinel-1 Interferometric Wide (IW) swath mode image acquired 14 November 2017 2122
 1161 UTC. Locations A-J identified. Level ice shown as thicker line (squares), rough ice as thinner
 1162 line (circles). Fast ice edge indicated by green line. (b) As (a) but for SIPL thickness under level
 1163 ice. (c) Five transects bounded by locations A-J, plotted against distance from coastal end of

1164 transect. Thickness measured downwards from snow/ice surface at zero. Consolidated level ice
 1165 thickness (h_Q) in brown, and consolidated ice thickness plus SIPL in blue (uncertainty indicated
 1166 by bar in panel E-F). Rough ice thickness (h_I) in orange. Second year ice shaded pink, regions
 1167 outside the fast ice edge shaded grey.

1168
 1169 **Figure 6.** Sea ice in front of Hells Gate Ice Shelf **(a)** In-phase apparent thickness (h_I) plotted on
 1170 Sentinel-1 Interferometric Wide (IW) swath mode image acquired 10 November 2017 1029
 1171 UTC. Locations A-F identified. Level ice shown as thicker line (squares), rough ice as thinner
 1172 line (circles). Fast ice edge indicated by green line. Ice older than 45 days is coastward of dashed
 1173 pale green line. **(b)** As (a) but for SIPL thickness under level ice. **(c)** Three transects, bounded by
 1174 locations A-F, plotted against distance from ice shelf front. Thickness measured downwards
 1175 from snow/ice surface at zero. Unsmoothed data shown in grey. All other data smoothed with
 1176 100 point median filter. Consolidated level ice thickness (h_Q) in brown, and consolidated ice
 1177 thickness plus SIPL in blue (uncertainty indicated by bar in panel E-F). Rough ice thickness (h_I)
 1178 in orange. Vertical dotted lines indicate boundaries identified from aerial photographs (see Fig 3
 1179 for transect A-B). Regions outside the fast ice shaded in grey, ice older than 45 days coastward
 1180 of green arrows. Core lengths of consolidated sea ice (magenta) and with estimates of SIPL
 1181 (cyan) for January 1994 and October 1995 (Tison et al., 1998).

1182
 1183 **Figure 7.** Gerlache Inlet and Silverfish Bay, Terra Nova Bay **(a)** In-phase apparent thickness (h_I)
 1184 plotted on Sentinel-1 Interferometric Wide (IW) swath mode image acquired 10 November 2017
 1185 1029 UTC. Locations A-J identified. Level ice shown as thicker line (squares), rough ice as
 1186 thinner line (circles). Drill hole thickness measurements on level ice shown by larger circles with
 1187 black rims. Fast ice edge indicated by green line. **(b)** As (a) but with SIPL thickness under level
 1188 ice. **(c)** Five transects bounded by points A-J plotted against distance from coastal end of
 1189 transect. Thickness measured downwards from snow/ice surface at zero. Consolidated level ice
 1190 thickness (h_Q) in brown, consolidated ice thickness plus SIPL in blue (uncertainty indicated by
 1191 bar in panel I-J). Rough ice thickness (h_I) in orange. Orange circular symbols with black rim are
 1192 drill hole measurements within 500 m of transects. Regions outside fast ice edge shaded grey.

1193
 1194 **Figure 8.** Northern Victoria Land coast **(a)** In-phase apparent thickness (h_I) plotted on Sentinel-1
 1195 Interferometric Wide (IW) swath mode images acquired 19 November 2017 1005 UTC and 20
 1196 November 2017 1536 UTC. Locations A-M identified. Level ice shown as thicker line (squares),
 1197 rough ice as thinner line (circles). Fast ice edge indicated by green line.
 1198 **(b)** Thickness plotted against distance from beginning of transect, locations A-M identified.
 1199 Thickness measured downwards from snow/ice surface at zero. Unsmoothed data shown in grey.
 1200 All other data smoothed with 100 point median filter. Consolidated level ice thickness (h_Q) in
 1201 brown, consolidated ice thickness plus SIPL in blue (uncertainty indicated by bar in top panel).
 1202 Rough ice thickness (h_I) in orange. Regions outside the fast ice edge shaded in grey.

1203
 1204
 1205

Fast Ice Thickness Distribution in the Western Ross Sea in Late Spring

P. J. Langhorne¹, C. Haas², D. Price³, W. Rack³, G. H. Leonard⁴, G. M. Brett³, and S. Urbini⁵

¹Department of Physics, University of Otago, Dunedin, New Zealand

²Alfred Wegener Institute for Polar and Marine Research, Bremerhaven, Germany

³Gateway Antarctica, University of Canterbury, Christchurch, New Zealand

⁴School of Surveying, University of Otago, Dunedin, New Zealand

⁵Istituto Nazionale di Geofisica e Vulcanologia, Roma, Italy

Contents of this file

Figures S1 to S2

Introduction

AEM fast ice (plus snow) thickness data in the western Ross Sea were collected between 8 and 13 November 2017 using airborne electromagnetic induction sounding. Thickness data have been partitioned into level and rough ice. In addition to consolidated ice plus snow thickness, under level ice the thickness of the sub-ice platelet layer was also found. The supplementary material contains the time-series of fast ice extent for the western Ross Sea from the dataset of Fraser et al., (2021) for the data shown in Fig. 2, and sample photographs of level and rough ice taken from the air.

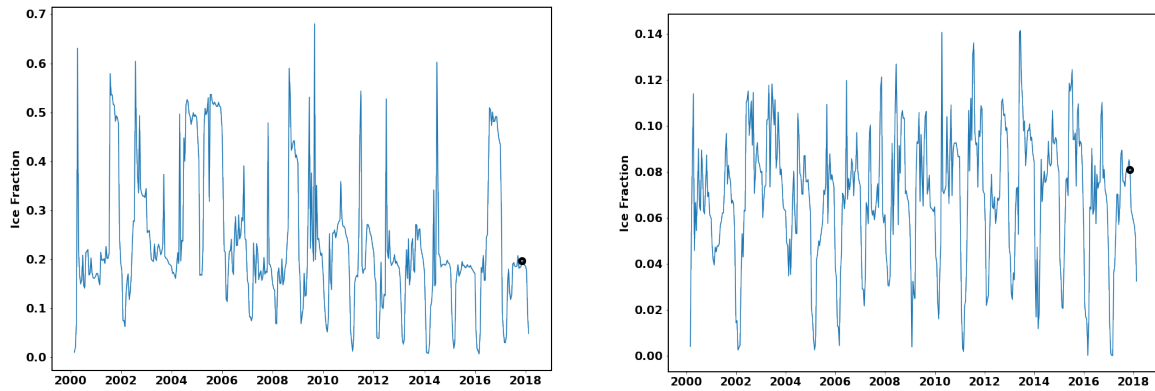


Figure S1. Time series of fast ice fraction from the Fraser et al. (2020) for **(a)** south of 75° S (see geographic area of Fig. 2a) and **(b)** north of 75° S (see geographic area of Fig. 2b). Fast ice fraction is defined as the number of pixels that contain fast ice divided by the possible number of pixels that could contain fast ice (i.e. all non-masked pixels from the Fraser et al. dataset). The pixel sizes are 1000 m x 1000 m. The dates of the AEM thickness surveys are indicated by black circles.



Figure S2 (a) Level ice in vicinity of Parker Ice Tongue between C and D of Fig. 8a&b (aircraft location 73.9101°S, 166.3555°E)
(b) Rough ice in Moubray Bay between L and M of Fig. 8a&b (aircraft location 71.9919 °S, 170.9110 °E)